JGR Oceans

RESEARCH ARTICLE
10.1029/2024JC021873

Special Collection:
The Arctic Ocean's changing Beaufort Gyre

The Arctic Beaufort Gyre in CMIP6 Models: Present and Future

Marylou Athanase[1], Raphael Köhler[2], Céline Heuzé[3], Xavier Lévine[4], and Ryan Williams[5]

[1]Climate Dynamics, Alfred Wegener Institute, Helmholtz-center for Polar and Marine Research, Bremerhaven, Germany, [2]Atmospheric Physics, Alfred Wegener Institute, Helmholtz-center for Polar and Marine Research, Potsdam, Germany, [3]Department of Earth Sciences, University of Gothenburg, Gothenburg, Sweden, [4]NORCE Norwegian Research Centre, Bjerknes Centre for Climate Research, Bergen, Norway, [5]British Antarctic Survey, Cambridge, UK

Abstract The Beaufort Gyre (BG) is an important feature of the Arctic Ocean. By accumulating or releasing freshwater, it influences ocean properties both within the Arctic and as far as the North Atlantic. Yet, its future remains uncertain: the gyre could strengthen as sea ice declines and allows increased wind stress on the ocean, or weaken along with the Beaufort High (BH) pressure system. Here, we provide a first evaluation of the BG in historical and climate-change simulations from 27 available global climate models. We find that the vast majority of models overestimate the gyre area, strength, and northward extent. After discarding the models with too inaccurate a gyre and its drivers—namely, the sea ice cover and BH—we quantify changes in the BG under two emission scenarios: the intermediate SSP2-4.5 and the high-warming SSP5-8.5. By the end of the 21st century, most models simulate a significant decline or even disappearance of the BG, especially under SSP5–8.5. We show that this decline is mainly driven by a simulated future weakening of the BH, whose influence on the BG variations is enhanced by the transition to a thin-ice Arctic. The simulated gyre decline is associated with an expected decrease in freshwater storage, with reduced salinity contrasts between the gyre and both Arctic subsurface waters and freshwater outflow regions. While model biases and unresolved processes remain, such possible stratification changes could shift the Atlantic-Arctic meridional overturning circulation northward.

Plain Language Summary Clockwise ocean currents accumulate comparatively fresh water over the Beaufort Gyre (BG), in the Amerasian Arctic Ocean. The future of that gyre, and whether it will hold or release the currently accumulated freshwater, is uncertain. Global climate models that supported reports from the Intergovernmental Panel on Climate Change (IPCC) can help shed light on such future climate questions. Using all models available, we select those that are capable of reasonably reproducing the Arctic BG. We find that most models predict that the gyre will shrink in a future warmer climate, in response to changes in the atmosphere. This gyre decline is predicted both under a high-emission scenario and under an intermediate "middle of the road" emission scenario. The BG region would no longer accumulate freshwater. This could impact future oceanic properties in the Arctic and in the North Atlantic.

Key Points:

- CMIP6 models generally simulate a too strong, large, and northward-extending Beaufort Gyre (BG) during the historical period
- Among the least unrealistic models, most simulations project a decline or disappearance of the BG by the end of the century
- As sea ice thins, the weakening Beaufort High drives gyre changes, and salinity contrasts are reduced between the gyre and Arctic outflows

Supporting Information:

Supporting Information may be found in the online version of this article.

Correspondence to:

M. Athanase and R. Köhler,
marylou.athanase@awi.de;
raphael.koehler@awi.de

Citation:

Athanase, M., Köhler, R., Heuzé, C., Lévine, X., & Williams, R. (2025). The Arctic Beaufort Gyre in CMIP6 models: Present and future. *Journal of Geophysical Research: Oceans*, *130*, e2024JC021873. https://doi.org/10.1029/2024JC021873

Received 19 SEP 2024
Accepted 24 FEB 2025

Author Contributions:

Conceptualization: Marylou Athanase, Raphael Köhler, Céline Heuzé, Xavier Lévine, Ryan Williams
Formal analysis: Marylou Athanase, Raphael Köhler, Céline Heuzé
Investigation: Marylou Athanase, Raphael Köhler, Céline Heuzé
Methodology: Marylou Athanase, Raphael Köhler, Céline Heuzé

1. Introduction

The Beaufort Gyre (BG) is a prominent feature of the Arctic Ocean, characterized by a large anticyclonic surface circulation pattern centered over the Canada Basin (Aagaard & Carmack, 1989), schematized in Figure 1. The gyre is primarily governed by winds associated with the Beaufort High (BH) pressure system (Proshutinsky & Johnson, 1997; Serreze & Barrett, 2011). The resulting surface stress leads to an accumulation of freshwater toward the center of the gyre through Ekman convergence (Proshutinsky et al., 2002, 2009, 2015). This freshwater accumulation not only influences ocean currents but also shapes the distribution of sea ice, heat, mass, ocean stratification, and nutrients in the Arctic (e.g., Solomon et al., 2021; Timmermans & Toole, 2023). The Arctic Ocean, in which the BG is embedded, forms a geographical link between the Atlantic and Pacific Oceans. Variations of the BG and its capacity to store freshwater therefore modulate water fluxes from the Arctic to lower latitudes. Importantly, freshwater release from the BG into the North Atlantic can temporarily hinder winter convection and impact the oceanic overturning circulation (Vellinga et al., 2008; J. Zhang et al., 2021). The anomalous freshening of the North Atlantic resulting from such release can also, in turn, influence large-scale atmospheric circulation regimes (D. Dukhovskoy et al., 2006; Proshutinsky et al., 2015).

Previous literature has documented the structure, variability, and past evolution of the BG using observations (e.g., Timmermans & Toole, 2023). The gyre exhibits a large interannual variability, alternating periods of

Validation: Marylou Athanase, Raphael Köhler, Céline Heuzé
Visualization: Marylou Athanase, Raphael Köhler, Céline Heuzé
Writing – original draft: Marylou Athanase, Raphael Köhler, Céline Heuzé
Writing – review & editing: Xavier Lévine, Ryan Williams

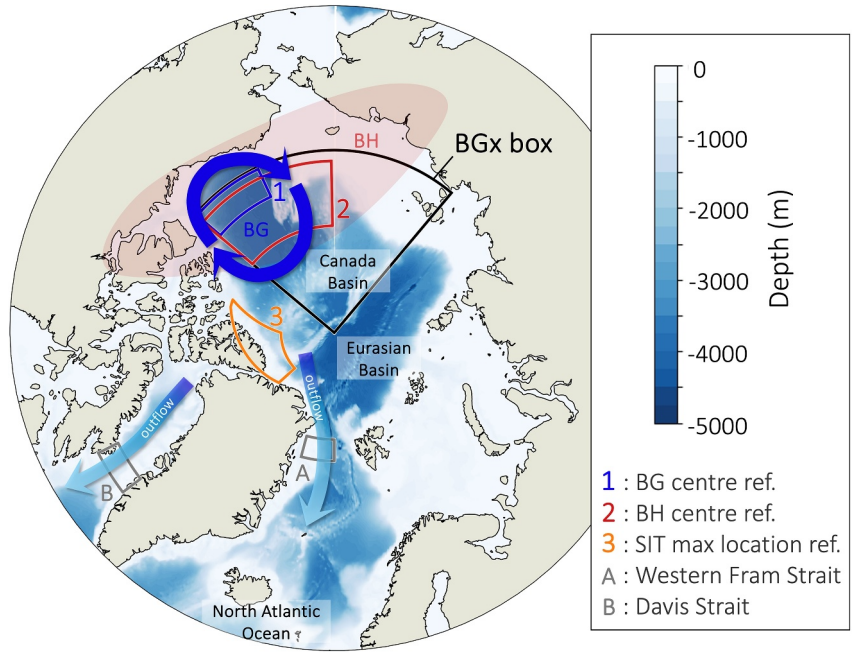

Figure 1. Bathymetry (background color) of the Arctic north of 60°N, from GEBCO Compilation Group, (2023). The Beaufort Gyre (BG, blue arrows) and Beaufort High (BH, red shade) are schematized. The so-called "BGx box," used in this study to describe the extended BG domain in CMIP6, is in black. Observation-based reference regions for the BG and BH centers and sea ice thickness maximum (SIT max) locations are indicated, respectively, by frames 1, 2, and 3. The western Fram Strait and Davis Strait regions, used for spatial comparisons of salinity in Section 3.4, are in gray frames A and B, respectively.

stagnation, and rapid changes (Proshutinsky et al., 2009, 2019). Despite this variability, satellite observations have indicated a notable increase in gyre freshwater content between 2003 and 2021, together with a northward area expansion (Proshutinsky et al., 2019; Rabe et al., 2011; Regan et al., 2019). This recent change is thought to result from intensified winds during the same period, and in general, seasonal and long-term gyre variability is attributed to changes in the atmospheric flow and BH properties (Proshutinsky et al., 2009; Regan et al., 2019). However, the transfer of wind energy to the ocean can be dampened by a compact sea ice cover, or enhanced over low sea ice concentrations via ice-ocean drag (Cole et al., 2017; Martin et al., 2014). Among other driving mechanisms, energy dissipation by ocean eddies (Doddridge et al., 2019; Manucharyan & Spall, 2016), variations in freshwater sources (Proshutinsky et al., 2019), large-scale modes of atmospheric variability (Morison et al., 2021; Proshutinsky et al., 2015), and the generation of Rossby waves (Zhao & Timmermans, 2018) can all also impact the BG.

The complex interplay between these processes means that the future of the BG is to date uncertain. The reduction in sea ice cover over the BG region (Mahoney et al., 2019) could increase the input of wind energy to the ocean; the expected transition to a seasonally ice-free Arctic Ocean would thus favor a strengthening of the BG (Armitage et al., 2020; Muilwijk et al., 2024). On the other hand, studies suggest a possible ongoing and future weakening of the BH pressure system (Karpechko et al., 2022; Moore et al., 2018; Smith et al., 2022). Such a decrease in sea-level pressure (SLP) and a weakening of the associated clockwise winds would have the opposite effect, causing the gyre to slow down. M. Zhang et al. (2024) also identify a negative trend in the winter BH index under the SSP2-4.5 and SSP5-8.5 scenarios. Notably, they find that while the decrease in SLP is robust, the vorticity of the winter BH remains constant or even intensifies. This dynamic response introduces additional uncertainty regarding the wind-driven forcing of the future BG, underscoring the need for further investigation into these interactions across temporal scales. How the BG may respond to these potentially counteracting sea ice and atmospheric pressure changes in a warmer climate remains so far unexplored, and is the focus of this study.

Here, we evaluate the present representation and future projections of the BG using models that participated in the Coupled Model Intercomparison Project Phase 6 (CMIP6) (Eyring et al., 2016). In the Arctic region, CMIP6

models have well-known biases in their representation of the sea ice cover (Notz & SIMIP Community, 2020) and full-depth oceanic properties (Heuzé et al., 2023; Khosravi et al., 2022; Muilwijk et al., 2023). Projections of future changes in freshwater storage are inconsistent across models at the pan-Arctic scale (S. Wang et al., 2022; Zanowski et al., 2021). Some models suggest a future strengthened stratification in the BG region (Muilwijk et al., 2023), likely caused by a projected increase in freshwater content forced by enhanced wind stress (Muilwijk et al., 2024). However, varying definitions of the BG domain and different model selections across existing studies make previous findings difficult to compare and interpret (see Muilwijk et al., 2023; Muilwijk et al., 2024; S. Wang et al., 2022; Zanowski et al., 2021). Furthermore, the specific representation of the BG in CMIP6 simulations has not been systematically investigated so far. Therefore, a comprehensive understanding of the gyre's future behavior in CMIP6 has yet to be established.

We carry out the first assessment of the BG representation in CMIP6 models and characterize its evolution in future climate projections. We describe the employed data and methods in Section 2. In Section 3, we evaluate the performance of 27 available models and select a subset of the least unrealistic models for projection analyses. We relate the gyre projections to its sea ice and atmospheric drivers, before briefly evaluating the impacts of future BG changes on water volume distribution and stratification at the pan-Arctic scale. We discuss our findings and provide concluding remarks in Section 4.

2. Data and Methods

2.1. CMIP6 Models

We use all ensemble members of all models that participated in the Climate Model Intercomparison Project phase 6 (Eyring et al., 2016) for which monthly fields of sea surface height above the geoid ("zos"), mean sea-level pressure ("psl"), and sea ice concentration ("siconc") are simultaneously available for the historical SSP2-4.5 and SSP5-8.5 runs (O'Neill et al., 2016). These are listed in Table 1. We limit the number of members to 10 to avoid large discrepancies between single-member models and large-ensemble simulations. When available, we also use the sea ice thickness ("sivol," which is more specifically the sea ice volume divided by grid cell area) or the sea ice mass ("simass"), with a preference for sivol as the density of ice is only provided by CanESM5 and UKESM1-0-LL. For the subset of models and ensemble members on which we perform the projection analysis, when available, we use the full-depth ocean practical salinity ("so") and potential temperature ("thetao").

We underline that broken links and challenges in accessing some of the CMIP6 data can be a recurring issue. For example, CIESM had to be eliminated from the projection analyses because part of the data fields were corrupted and not available on Earth System Grid Federation (ESGF). We emphasize the critical need for reliable data access even years after their upload to ESGF.

2.2. Observational Products

To investigate the historical representation of the BG and its drivers in CMIP6 models, we use a set of observational products and literature-based references. So far, no database or product of the observed BG properties is available. We thus use monthly satellite-derived data from Regan et al. (2019) (their Figure 2) as the observational reference of the historical gyre characteristics (leftmost three columns in Figure 2a). Regan et al. (2019) employed altimetry-derived fields of dynamic ocean topography (DOT), spanning the 2003–2014 period with monthly resolution. Note that their DOT fields are derived from Envisat data for 2003–2011 and from CryoSat-2 data for 2012–2014 (Armitage et al., 2017). DOT is not directly comparable to the modeled "zos," notably because "zos" is the purely nonsteric component of sea surface height, the inverse-barometer effect has been removed, and "zos" uses a different definition of the geoid. For more specific information, the reader should refer to Griffies et al. (2016).

For the BH, we employ monthly mean sea-level pressure (SLP) data from the ERA5 reanalysis (Hersbach et al., 2020). The evaluation is done for the last 30 years of the historical period, that is, 1985–2014.

Finally, we use the monthly sea ice thickness (SIT) available in Kwok (2018). As detailed in Kwok (2018), this product originates from the CryoSat-2 satellite measurements and is therefore limited to 2011–2015. Besides, they do not include the ice melting period, further limiting them to the months from October to April. We chose this now-outdated product for model validation as it would have been state of the art when the modelers were initializing and especially so tuning their model. We also use the longer record of monthly mean sea ice

Table 1
Description of the 27 CMIP6 Models Used in This Study

Model name	Members	Ocean	Sea Ice	Ocean/Ice Res.	Atmosphere	Atmosphere Res.
ACCESS-CM2	3	MOM5	CICE5.1.2	100 km, z* 50	MetUM-HadGEM3-GA7.1	250 km
AWI-CM-1-1-MR	1	FESOM 1.4	FESOM 1.4	25 km, z* 46	ECHAM6.3.04p1	100 km
BCC-CSM2-MR	3	MOM4	SIS2	50 km, z 40	BCC_AGCM3_MR	100 km
CAMS-CSM1-0	3	MOM4	SIS1.0	100 km, z 50	ECHAM5_CAMS	100 km
CanESM5	10	NEMO 3.4.1	LIM2	100 km, z 45	CanAM5	500 km
CIESM	3	CIESM-OM	CICE4	50 km, z 46	CIESM-AM	100 km
CMCC-CM2-SR5	1	NEMO 3.6	CICE4.0	100 km, z* 75	CAM5.3	100 km
CMCC-ESM2	1	NEMO 3.6	CICE4.0	100 km, z* 75	CAM5.3	100 km
CNRM-CM6-1	6	NEMO 3.6	Gelato 6.1	100 km, z* 75	Arpege 6.3	250 km
CNRM-CM6-1-HR	1	NEMO 3.6	Gelato 6.1	25 km, z* 75	Arpege 6.3	100 km
EC-Earth3	1	NEMO 3.6	NEMO-LIM3	100 km, z* 75	IFS cy36r4	100 km
EC-Earth3-CC	1	NEMO 3.6	NEMO-LIM3	100 km, z* 75	IFS cy36r4	100 km
EC-Earth3-Veg	2	NEMO 3.6	NEMO-LIM3	100 km, z* 75	IFS cy36r4	100 km
EC-Earth3-Veg-LR	1	NEMO 3.6	NEMO-LIM3	100 km, z* 75	IFS cy36r4	250 km
FIO-ESM-2-0	3	POP2-W	CICE4.0	100 km, z 61	CAM4	100 km
GFDL-ESM4	1	GFDL-OM4p5	GFDL-SIM4p5	50 km, ρ-z* 75	GFDL-AM4.1	100 km
HadGEM3-GC31-LL	2	NEMO-HadGEM3-GO6.0	CICE-HadGEM3-GSI8	100 km, z* 75	MetUM-HadGEM3-GA7.1	250 km
INM-CM4-8	1	INM-OM5	INM-ICE1	100 km, σ 40	INM-AM4-8	100 km
INM-CM5-0	1	INM-OM5	INM-ICE1	50 km, σ 40	INM-AM5-0	100 km
IPSL-CM6A-LR	3	NEMO 3.6	NEMO-LIM 3	100 km, z* 75	LMDZ	250 km
MIROC6	3	COCO4.9	COCO4.9	100 km, σ-z 62	CCSR AGCM	250 km
MPI-ESM1-2-HR	2	MPIOMI 1.6.3	N/A	50 km, z 40	ECHAM6.3	100 km
MPI-ESM1-2-LR	10	MPIOMI 1.6.3	N/A	250 km, z 40	ECHAM6.3	250 km
MRI-ESM2-0	1	MRI.COM 4.4	MRI.COM 4.4	100 km, z* 60	MRI-AGCM3.5	100 km
NorESM2-LM	1	BLOM (MICOM)	CICE5.1.2	100 km, ρ-z 53	CAM-OSLO	250 km
NorESM2-MM	1	BLOM (MICOM)	CICE5.1.2	100 km, ρ-z 53	CAM-OSLO	100 km
UKESM1-0-LL	8	NEMO-HadGEM3-GO6.0	CICE-HadGEM3-GS18	100 km, z* 75	MetUM-HadGEM3-GA7.1	250 km

Note. From left to right: model name, number of members used in this study, ocean model component, sea ice model component, native nominal resolution of the ocean and sea ice grid along with the vertical grid type (ρ means isopycnic, σ terrain-following, and several symbols a hybrid grid) and number of levels, atmosphere model component, and native nominal resolution of the atmosphere grid. The detailed references of the data sets can be found in Table S1 in Supporting Information S1.

concentration (SIC) from January 1985 to December 2014 available via the Copernicus Data Store. Until August 2007 included, this SIC data were provided by the Ocean and Sea Ice Satellite Application Facility (OSI SAF) 409a data set, and from September 2007 onward by the OSI SAF operational data set. For more information about both products, see Lavergne et al. (2019).

2.3. Methods

CMIP6 monthly mean ocean, sea ice, and atmosphere fields were regridded onto a common global 0.5° × 0.5° grid for all models. We used a bilinear interpolation for all models except the AWI-CM-1-1-MR ocean fields, for which we used conservative remapping following Semmler et al. (2020). Interpolating the model data is necessary to enable intermodel comparisons. No budget or flux calculation is done in our analyses, hence justifying the use of interpolated fields rather than native model grids.

Climatological means are derived from CMIP6 simulations by averaging monthly data over 30-year periods: 1985–2014 for historical runs and 2070–2099 for SSP2-4.5 and SSP5-8.5 scenarios. Monthly time series used for correlation analyses are low-pass filtered with a 24-month cutoff frequency using a Butterworth filter. In the

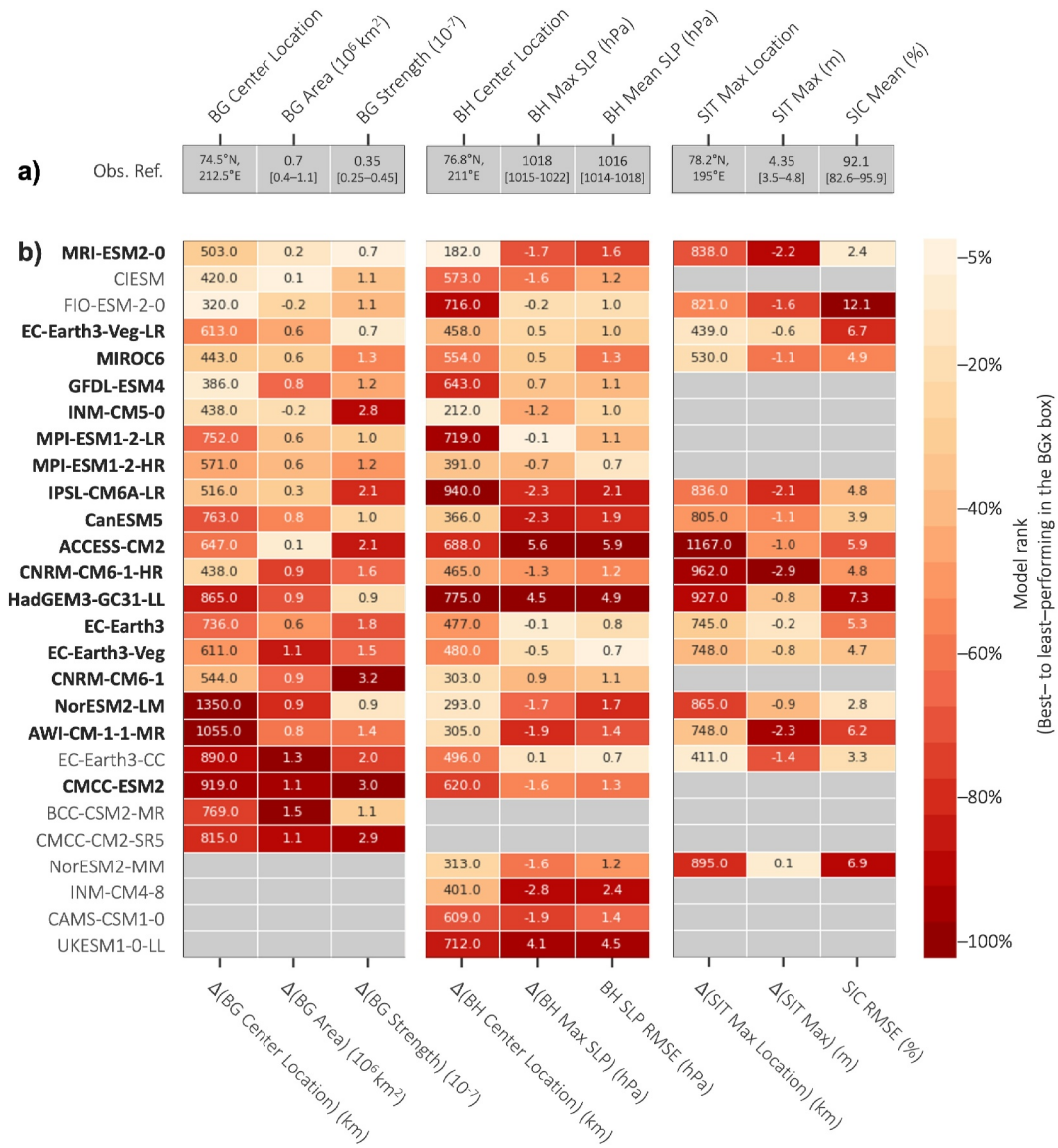

Figure 2. (a) Observation-based reference properties of the annual average Beaufort Gyre (BG), Beaufort High (BH), and sea ice cover in the BGx box (see Methods). BGx indicates the extended BG domain, as shown in Figure 1. For all parameters except location, intervals in brackets indicate the complete range of interannual variability in the observational products. (b) Ensemble-average performance of each model in representing the BG, BH, and sea ice cover in the BGx box: the symbol Δ at the bottom of the panel indicates a difference between the model 1985–2014 mean and the corresponding observational reference. Note that observational references can be derived over varying time intervals (see Methods). For the Beaufort High sea-level pressure (BH SLP) and the sea ice concentration (SIC), root mean squared error over the BGx box between the two temporal means are presented. The model rank is in color, with the best-performing model representing the top 5%. Grayed boxes indicate that the model has no BG, no Beaufort High, or no realistic sea ice distribution. The overall model list is ordered from best (top) to worst (bottom) performance based on their average ranks in BG metrics (leftmost three columns). Models used for subsequent projection analyses are highlighted in bold.

following, we define metrics to characterize the BG, its drivers, and upper-ocean properties in CMIP6 models. Climatological means of these metrics are based on the corresponding metric monthly time series, which is particularly important for BG. Indeed, detecting, for example, the gyre center and extent on monthly fields prevents artificial smoothing of SSH fields, avoiding inaccurate estimates of gyre properties.

To examine the properties of the BG and its drivers, we use a box bounded by longitudes 140°E–230°E and latitudes 73°N–90°N (black box, Figure 1). We hereafter refer to this region as the reference "BGx box," used

here to describe the extended BG domain. Our BGx box is larger than regions defined in previous observational studies (Kenigson & Timmermans, 2021; Regan et al., 2019; Serreze & Barrett, 2011), in order to capture the larger CMIP6 multimodel variability than existing observations.

2.3.1. Metrics of the Beaufort Gyre Properties

We define the center of the BG as the location of the maximum SSH within the BGx box defined above. We estimate the distance from the observed BG center as the shortest distance between the simulated position and the reference region comprising observed values. If the simulated position is found within the reference region, the distance is set to 0 km. The BG extent is in turn detected as the largest closed contour of SSH enclosing the BG center, in agreement with past studies (Bertosio et al., 2022; Proshutinsky et al., 2009; Regan et al., 2019). To describe and evaluate the BG state in the CMIP6 simulations, we compute metrics of the gyre area and strength following Regan et al. (2019). The BG area is the total area enclosed by its extent contour, expressed in million square kilometers. The strength S is computed as

$$S = \frac{SSH_{\max} - SSH_{\min}}{R}, \quad (1)$$

where $SSH_{\max}$ is the maximum SSH at the gyre center, $SSH_{\min}$ is the SSH along the gyre contour, that is, at the gyre edge, and R is the radius of the gyre. We use the mean radius of the gyre, as using either the minimum, maximum, or median radius does not notably affect variations of S, and solely shifts the resulting time series (Regan et al., 2019). Note that we derive the gyre strength from SSH fields, while Regan et al. (2019) use DOT fields. By definition, this leads to values of strength one order of magnitude lower in our SSH-based computations than their DOT-based results. This does not impact short-to long-term relative strength variations. To provide a reference value comparable to the CMIP6 gyre strength, we divide by 10 values from Regan et al. (2019). Note that gyre strength is set to zero for months during which the gyre area is detected to be so small (threshold of 0.5 million square kilometers) that the gyre is considered nonexistent.

2.3.2. Drivers of the Beaufort Gyre: Beaufort High and Sea Ice Cover

Analogous to the gyre location, the center position of the BH is defined as the location of the maximum monthly SLP in the BGx box. Distance to the observed BH center is estimated as for the BG center (Section 2.3.1). The value of this SLP maximum is an indicator of the BH intensity. Observation-based references of the BH center and maximum SLP are derived from ERA5, for the climatological period 1985–2014. We also examine the overall CMIP6 representation of the SLP in our region of interest. To do so, we calculate the root mean squared error (RMSE) of the climatological mean fields between the modeled and ERA5 fields within the BGx box. The ERA5 yearly mean SLP in the BGx box is provided for reference and compared to the RMSE amplitude.

As an indicator of the models' capability to realistically simulate the Arctic sea ice cover, we detect the pan-Arctic yearly maximum SIT from the monthly thickness output, in both CMIP6 models and in the observations from Kwok (2018). Distance to the observed location of the SIT maximum is derived as for the gyre center (Section 2.3.1). A reference region for a realistic location of the SIT maximum is inferred from a visual inspection of the satellite-derived data, with the thickest ice found along the Greenland coastline (Kwok, 2018, their Figure 3) as defined in Figure 1. Finally, we evaluate the models' representation of the mean SIC in the BG domain by calculating the RMSE of SIC within the BGx box, and we provide the mean SIC in the box for reference.

For the models selected for the projection analyses, we compute their sea ice volume in the BGx box by multiplying "sivol" (interpolated on the common $0.5° \times 0.5°$ grid) by the $0.5° \times 0.5°$ grid cell area and summing over the entire area of the box. We also compute the volumes of specific SIT classes ranging from 0 to 5 m with 1-m intervals, that is for grid cells with a thickness ("sivol") for example,.

- larger or equal to 2 m and strictly lower than 3 m (thickness class 2–3 m);
- larger or equal to 1 m and strictly lower than 2 m (thickness class 1–2 m).

These two thickness classes, 2–3 m and 1–2 m, are employed hereafter to determine the timing of the transition from the previously dominating thicker ice to a thinner, below 2 m-thick cover (cf. Figure S1 in Supporting Information S1). The date of this so-called "2 m ice transition" for each simulation is derived as the first year

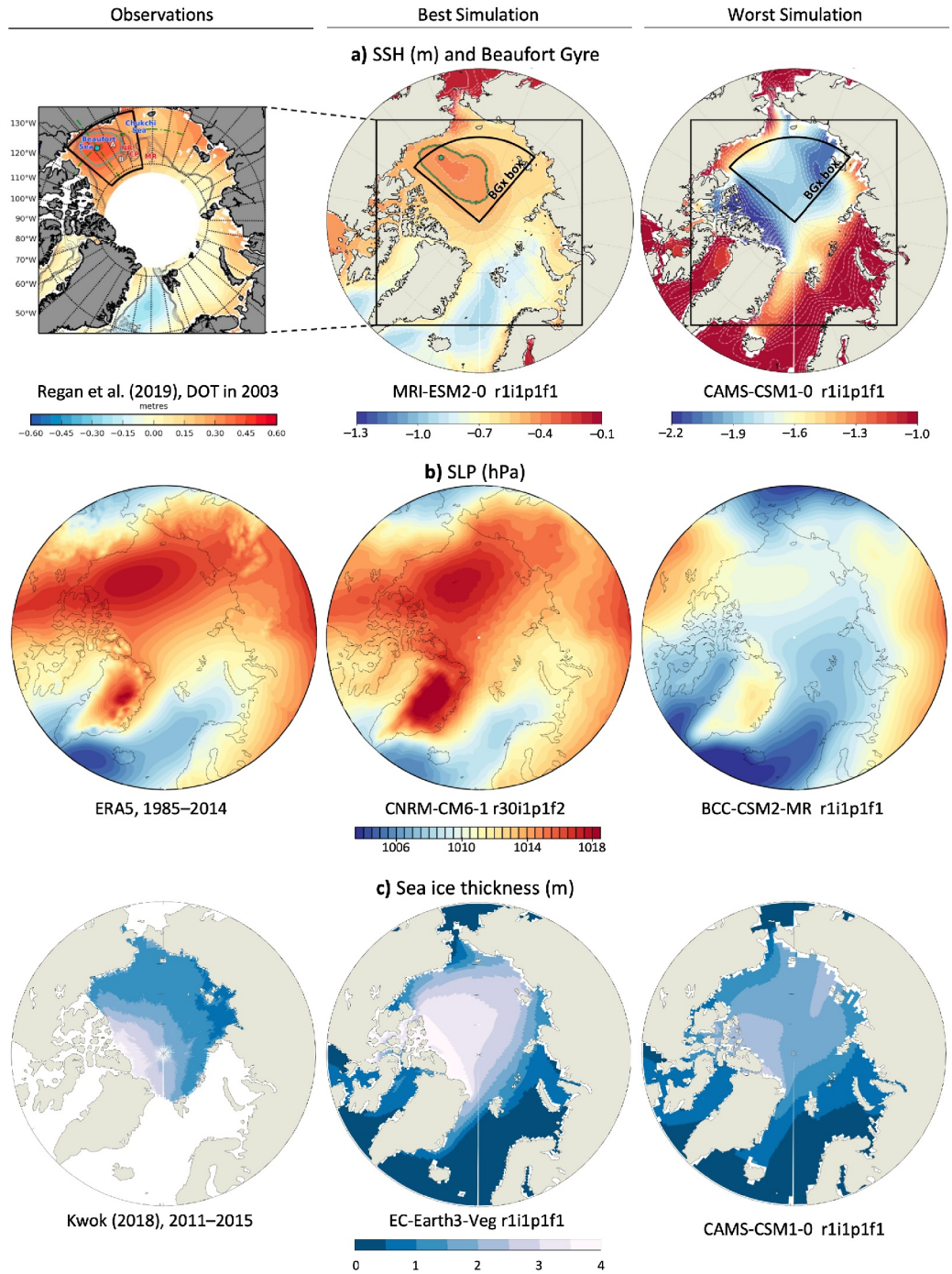

Figure 3. Observational values (left) and 1985–2014 mean modeled value from the best (center) and worst (right) simulations, for panel (a) the sea surface height, (b) the sea-level pressure, and (c) the sea ice thickness (SIT). In panel (a), note the different color scales for all three panels due to the different ranges in all fields, despite similar water volume relative distributions for the left and center panels. In the absence of an observational product, observations for the sea surface height show instead the dynamic ocean topography in 2003 (scale between −0.60 and 0.60 m) as in Regan et al. (2019); panel reproduced with permission, license number 5815871025945. Similarly, the SIT observations are limited to October–April, in 2011–2015 only, as in Kwok (2018).

where the 2–3 m class systematically has a lower volume than the thinner 1–2 m class. Other pairs of ice classes were tested, but the 2-m thickness cutoff yielded the strongest results in terms of its effect on the BG. Based on the sea ice rheology formulation of Hibler III (1979), most CMIP6 models are parametrized to modulate air-sea

momentum fluxes using sea ice cover rather than thickness. As described in the Supporting Information S1 of Manucharyan and Thompson (2022), this formulation introduces a critical SIC below which the sea ice is approximately in free drift. This threshold depends on the critical rheology parameter C*, which is empirically set to 20 in current general circulation models (GCMs) using this approach. Consequently, sea ice transitions to free drift below a concentration threshold of approximately 80% (Figure S3 in Supporting Information S1 of Manucharyan and Thompson (2022)). In our study, we adopt a physically somewhat more plausible SIT-based threshold. One notable advantage is that thickness changes more slowly than concentration, making it easier to detect the regime shift, whereas the strong seasonal cycle of concentration introduces additional complexity in selecting the optimal month for analysis. We further note that the 2-m thickness transition also aligns closely with the timing of the regime shift to the 80% SIC threshold.

2.3.3. Upper-Ocean Properties

To quantify the impact of changes in the BG on Arctic Ocean properties, we compute the salinity in and below the halocline, in the BG, and in the Fram and Davis straits. The halocline depth is computed from the 30-year mean potential temperature θ and practical salinity S, using the same method as in Heuzé and Liu (2024), adapted from Shu et al. (2022). The halocline depth is the first depth level z where

$$\alpha \frac{\partial \theta}{\partial z} / \beta \frac{\partial S}{\partial z} \geq 0.05, \tag{2}$$

where α and β are the thermal expansion and haline contraction coefficients, respectively. We then take the mean salinity from the surface to the halocline depth, as well as the difference between that mean salinity and the salinity two depth levels below the halocline as a proxy for local stratification strength. This value of two levels comes from this group's experience with CMIP6 models in the Arctic Ocean (e.g., Heuzé et al. (2023)): Depending on the biases in stratification in that model and on the location, one level below the detected depth may still be in the halocline, that is, in the depth range over which salinity changes rapidly, whereas two levels below is near-certainly in a different water mass, as intended. It is worth noting that although the number of vertical levels varies between 40 and 75 in our model selection (Table 1), the halocline is an upper-ocean feature encountered in the depth range close to the surface where the models have a similar approx. 10-m vertical resolution. The differences in halocline depth between models are more attributable to model biases in stratification than in vertical resolution (e.g., Muilwijk et al. (2023)). Varying the number of levels, or choosing a fixed distance and therefore having to interpolate the models vertically, does not significantly change the results (not shown), as we are interested in the across-model relationships. It also yields results that are consistent with those of Muilwijk et al. (2023), despite the simplicity of our method.

The salinity values are then spatially averaged over three regions (see Figure 1), chosen for consistency with Bertosio et al. (2022).

- for the BG, longitudes 140°E–230°E and latitudes 73°N–90°N, that is the BGx box as in the rest of this manuscript. This gives similar results to using the actual centers of the BG for each model and scenario (not shown) and is a more robust approach to work with the models whose BG disappears during the warming scenarios.
- for the western Fram Strait, longitudes 345°E–0°E and latitudes 78°N–80°N.
- for Davis Strait, longitudes 297°E–307°E and latitudes 65.5°N–67.5°N.

In the two outflowing straits, if no halocline depth can be found with the method described above, the depth is set to 200 m—a depth usually described as the deepest average lower boundary of the halocline in these regions (see e.g., Muilwijk et al., 2023; Polyakov et al., 2018; Rudels et al., 2004).

Note that although many papers refer to the freshwater content of the BG (see Introduction), we chose not to compute any freshwater content and use the salinity instead. This is because the computation of the freshwater requires a reference salinity, which is debated practice when working with observations (Schauer & Losch, 2019) and is near-impossible for CMIP6 models, with their respective biases, especially so when looking at several warming scenarios as we do here.

3. Results

3.1. Historical Assessment

We evaluate the capability of CMIP6 models to realistically represent the historical BG. We assess the performance of the models based on the metrics of the BG, BH, and sea ice fields as defined in the Methods section. Model metrics are averaged over the historical period 1985–2014, and compared to observational values over the reference BGx box defined in the Methods (Figure 2). We sort models based on their ensemble-average ranks in the BG metrics (leftmost three columns in Figure 2). Examples of the mean SSH, SLP, and SIT from the best- and worst-performing simulations are shown in Figure 3.

The representation of the BG is highly variable across models (leftmost three columns in Figure 2). This is consistent with previous literature, which identified a large intermodel spread in Canadian Arctic ocean properties in CMIP6 (Muilwijk et al., 2023; S. Wang et al., 2022; Zanowski et al., 2021). We find that 4 out of 27 models fail to simulate any gyre circulation (gray boxes in Figure 2b). The resulting SSH patterns are unrealistic (Figure 3a). Models that do simulate a BG predominantly overestimate the gyre area, and all overestimate its strength with instances of modeled mean values up to 10 times larger than observations (see e.g. CNRM-CM6-1). As the gyre is bounded to the south by the continental coast, this overestimated area coincides with a simulated BG location too far north in the central Arctic. This is true even for the best-performing models, such as MRI-ESM2-0 (Figure 3a). No apparent link was found between model resolution and accurate representation of the gyre.

The primary driver of the BG (e.g., Kelly et al., 2019), the BH pressure system is in contrast generally well represented in CMIP6 models. So far, the CMIP6 models have demonstrated reasonable skill in simulating the Arctic winds and cyclones (J.-N. Song et al., 2021; X. Wang et al., 2023; Zapponini & Goessling, 2024): a realistic representation of the Arctic BH and overall pressure field is thus in logical agreement with such previous findings. Here, only two models do not simulate distinct BH patterns, BCC-CSM2-MR and CMCC-CM2-SR5 (gray boxes in Figure 2b). For all other models, the BH mean center location is within the BGx reference region, and is found less than 500 km from the average BH location in ERA5 for most models. The simulated SLP field is generally realistic, with maximum values close to observations and moderate RMSE. Although most models tend to simulate a too-weak maximum, a majority of models have their SLP maximum within the range of the smallest and largest yearly SLP maximum of ERA5. Exceptions are the models ACCESS-CM2, HadGEM3-GC31-LL, and UKESM1-0-LL, which stand out notably with differences in maxima and RMSE of the temporal means of more than 4 hPa.

In contrast, we find that the representation of Arctic SIT in CMIP6 is often inaccurate, in agreement with for example, Notz and SIMIP Community, (2020). For 11 out of 27 models, we consider the spatial distribution of SIT unacceptable. Examples of this spatial distribution are given in Figure 3c. The observed SIT values (left) cover only the last 5 years of the historical run, when the real-world sea ice had already thinned (IPCC, 2019). Therefore, we tolerate modeled sea ice values up to 1 m thicker than observed, as long as the spatial pattern is respected, as in our best model example (middle). In the worst simulation, not only is the ice too thin but there is also a thick ice tongue extending into the central Arctic from Siberia, thin ice from Svalbard to North Greenland, and the entire Greenland Sea is ice-covered year-round down to Iceland. Finally, the sea ice in CIESM could not be assessed because the sea ice files were not available on ESGF. For the remaining models, which do not feature an unrealistic pan-Arctic distribution of SIT, we evaluate the sea ice in the BG region (Figure 2b, last three columns). The simulated thickness maximum in the gyre region is generally underestimated and located too far northeast of that observed. The SIC in the BG area is better represented in CMIP6 models than the SIT, with RMSE lower than 10% and often lower than 5% (Figure 2, last column). A notable exception is FIO-ESM-2-0, with the largest RMSE (12%) in the gyre area, and we note that this model accumulates sea ice up to 30-m thick in a channel of the Canadian Archipelago (not shown).

This historical assessment allows us to select adequate models for our projection analyses. We discard the 4 models failing to simulate a BG (NorESM2-MM, INM-CM4-8, CAMS-CSM1-0, and UKESM1-0–LL), as well as the 2 models that do not accurately represent both the BH and sea ice (BCC-CSM2-MR and CMCC-CM2-SR5). We further exclude 3 additional models. First, FIO-ESM-2-0 is one of the best-performing models in terms of BG metrics but is excluded due to its unrealistic thick sea ice accumulation. CIESM had to be eliminated from the projection analyses because part of the data fields were corrupted and not available on ESGF. Finally, EC-Earth3-CC exhibits the lowest rank of all four EC-Earth3 models considered here. To avoid the over-

representation of the EC-Earth3 model family in our analyses, we discard EC-Earth3-CC and retain the three other EC-Earth3 models. We emphasize that the models used here for further analyses are not without limitations, and those limitations are outlined when drawing conclusions hereafter. The 18 models used for projection analyses are indicated with bold fonts in Figure 2b.

3.2. The Beaufort Gyre Under Two Warming Scenarios

Despite the increase in BG area observed in the 2000s–2010s, previous literature pointed out large uncertainties regarding the future of the gyre (e.g., Timmermans & Toole, 2023). The declining sea ice cover is expected to increase wind energy input to the ocean, favoring a stronger BG (Armitage et al., 2020). On the other hand, studies suggest a possible weakening of the BH pressure system, which could rather lead to a gyre dampening (Moore et al., 2018; Smith et al., 2022). Here, we examine the projected BG characteristics under two warming scenarios: the intermediate SSP2-4.5 and the high emissions SSP5-8.5. We show the historical and projected mean gyre area, strength, and location for each model, as well as the multimodel distributions in Figure 4 (respectively, upper and lower panels).

We find that a large majority of CMIP6 models shows a strong decline in BG area toward the end of the century (Figure 4a). Both SSP2-4.5 and SSP5-8.5 projected multimodel distributions are significantly lower than the historical one, with a 99.95% confidence level according to a two-sided Wilcoxon test. Under the high-warming scenario SSP5-8.5, all models except ACCESS-CM2, INM-CM5-0, and MPI-ESM1-2-LR, that is, 15 out of the 18 analyzed models, exhibit a decrease in the gyre area (Figure S2 in Supporting Information S1). Importantly, for 10 of them, the BG disappears: for at least one member, their 30-year average area falls below a threshold of 0.5 million square kilometers, that is, below the first percentile of the historical area multimodel distribution and the lower range of observed historical values (0.4–1.1, Figure 2a). To the exception of MRI-ESM2-0, these 10 models include all 9 NEMO-based models considered here for projection analyses: CanESM5, CMCC-ESM2, CRNM-CM6-1, CRNM-CM6-1-HR, EC-Earth3, EC-Earth3-Veg, EC-Earth3-Veg-LR, HadGEM3-GC31-LL, and IPSL-CM6A-LR. Note that the amplitude of these changes is not sensitive to the season in which they are considered.

The timing of the gyre disappearance however differs across these models, as indicated by the large intermodel spread in Figure 5. CanESM5, CNRM-CM6-1, and IPSL-CM6A-LR simulate the most rapid area decline, losing their gyre in the 2030–40s (Figure S2 in Supporting Information S1). On the other hand, EC-Earth3 and EC-Earth3-Veg stand out as the only models exhibiting a temporary area increase in the 2000–50s before a delayed gyre disappearance in the 2070s (Figure S2 in Supporting Information S1). In the intermediate warming scenario SSP2-4.5, the multimodel area decline is significantly smaller than in the SSP5-8.5 (at the 99% confidence level). The majority of models (12 out of 18) still show a reduction in gyre area. Exceptions are AWI-CM-1-1-MR and GFDL-ESM4, which project no notable change in SSP2-4.5, and NorESM2-LM, which projects a mild area increase. However, the SSP2-4.5 projected predominant area decline stagnates in the second half of the century (Figures 5a and 5b), and only four models show a disappearance of the BG under this more moderate warming scenario (Figure 4a): CanESM5, IPSL-CM6A-LR, EC-Earth3, and MRI-ESM2-0. While 3 of these models are NEMO-based, previous research showed that these models strongly differ by their representation of historical ocean stratification (Muilwijk et al., 2023), sea ice, and freshwater storage (Zanowski et al., 2021); thus, no evident common explanation is found for their rapid gyre disappearance.

In most models, the BG declines or even disappears: only 3 out of 18 models do not feature an area decrease in either scenario. Of these remaining 3 models, MPI-ESM1-2-LR simulates little change to its nearly pan-Arctic gyre, with an ensemble mean value and spread remaining similar throughout the entire 1970–2100 period (Figure 5c and Figure S2r in Supporting Information S1). The other two, ACCESS-CM2 and INM-CM5-0, show an expansion of the BG area in both scenarios, with the spread between models and individual members increasing with time (Figure 5d and Figures S2a and S2n in Supporting Information S1).

We note that in all models where the BG declines, the historical mean area is overestimated, implying a greater potential to simulate larger area declines. These models nevertheless do capture the observed area increase in the 2000s–2010s to some extent, despite large intermodel variability (Figures 5a and 5b). In contrast, the two outlier models projecting a gyre increase, ACCESS-CM2 and INM-CM5-0, feature mean gyre areas consistent with the observations (Figure 5d). They however fail to reproduce the observed increasing trend in the 2000s–2010s and significantly overestimate the mean gyre strength (see Figure 2). Additionally, ACCESS-CM2 simulates a highly variable BG area, shape, and location at monthly timescales during the historical period (not shown). It is thus

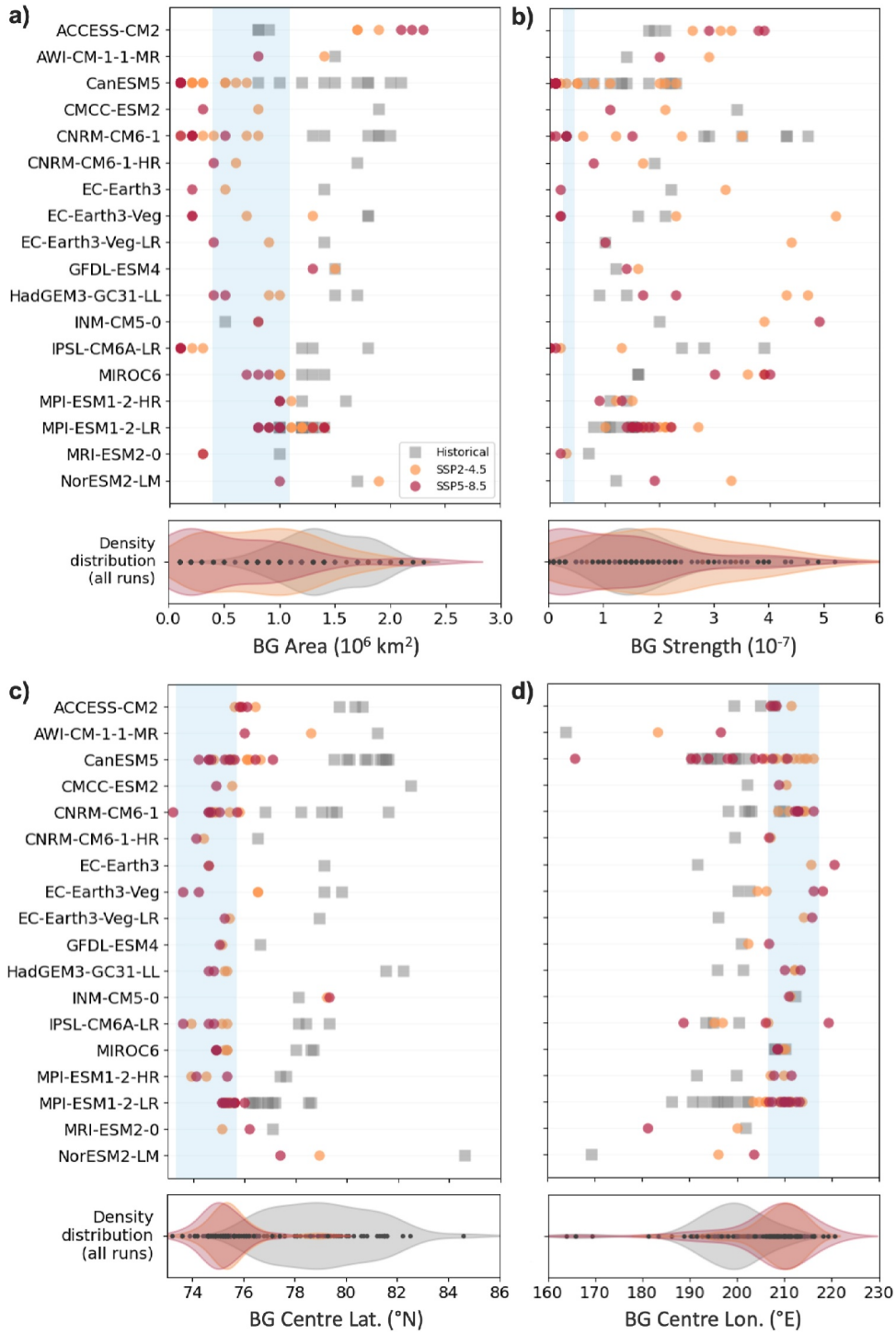

Figure 4. Beaufort Gyre (a) area $\left(10^6\ \mathrm{km}^2\right)$, (b) strength $\left(10^{-7}\right)$, (c) center location latitude (°N), and (d) center location longitude (°E), in the SSP2-4.5 (orange) and SSP5-8.5 (red) scenarios compared to the historical period (gray), averaged for each metric over the last 30 years of the monthly time series. For a monthly gyre area below the gyre-disappearance threshold of $0.5 \times 10^{12}\ \mathrm{m}^2$, the gyre strength is set to zero and the gyre center location is not detected. Parameters for each model and their member(s) are detailed in the upper panels, with ranges of annual observed values from Regan et al. (2019) reported in blue shades. Density distributions for all considered runs (all models and their members) in each scenario are in the lower panels. Note that dots can overlay each other.

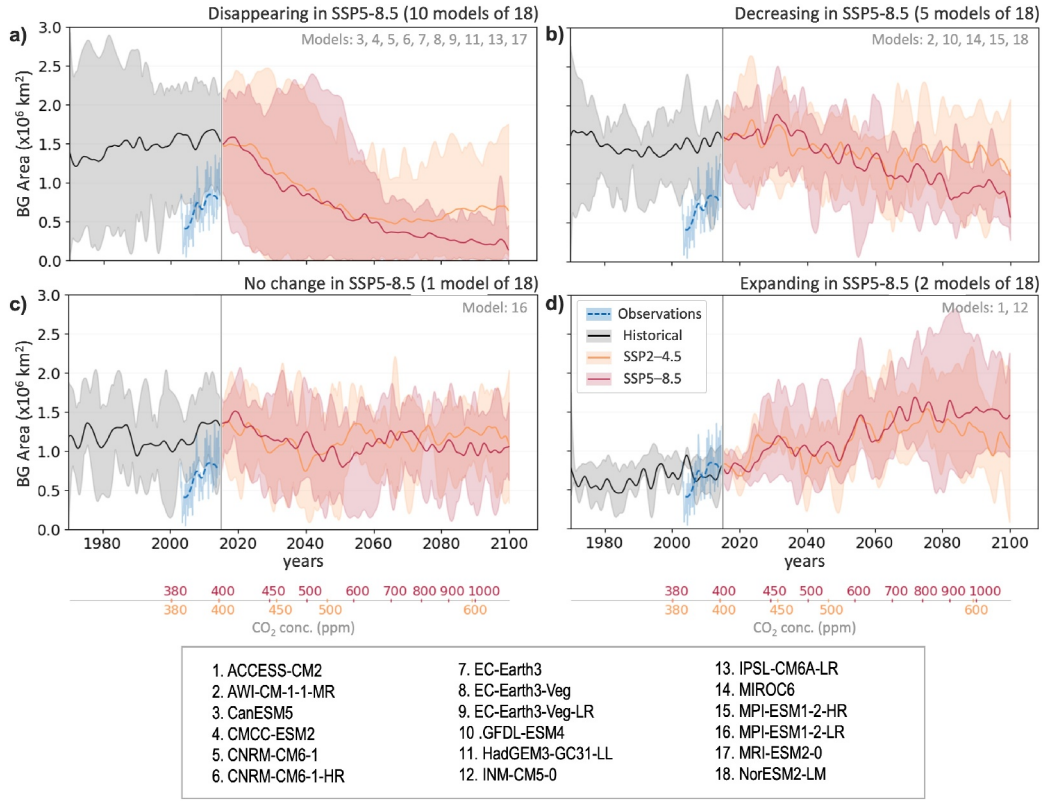

Figure 5. Time series of the historical and projected Beaufort Gyre (BG) area $\left(10^6\ \mathrm{km}^2\right)$ in the CMIP6 simulations under historical (black), SSP2-4.5 (orange), and SSP5-8.5 (red) scenarios. The multimodel mean and spread are in bold lines and shaded envelopes, respectively. Models (and their individual members) are grouped according to their behavior in the SSP5-8.5 scenario in Figure 4a, namely, (a) a disappearing BG, (b) a decreasing BG area, (c) no area change, and (d) an increase BG area. Monthly data for each member are low-pass filtered with a 24-month cutoff frequency. Monthly observations from Regan et al. (2019) for 2003–2014 are reported in each panel (blue), both unfiltered (shaded lines) and low-pass filtered with the same 24-month cutoff frequency (dashed lines). CO_2 concentrations for both scenarios are from Meinshausen et al. (2020). CMIP6 models included in each panel are indicated by a number.

probable that this model features some inaccuracies in its representation of the gyre dynamics, which may lead to inaccurate projections.

Unsurprisingly, projected changes in the strength of the BG are linked to its disappearance or maintenance (Figure 4b). By definition, the gyre strength is considered zero for months during which the gyre is not present (see Methods). The predominant disappearance of the gyre projected in the SSP5-8.5 scenario is thus reflected in the multimodel distribution large strength decrease, significant at the 99% confidence level (Figure 4b, lower panel). In contrast, if their simulations project the persistence of a BG, 10 of the 18 models have an increase in gyre strength (ACCESS-CM2, AWI-CM1-1-MR, EC-Earth3, EC-Earth3-Veg and EC-Earth3-Veg-LR, GFDL-ESM4, HadGEM3-GC31-LL, INM-CM5-0, MIROC6, and NorESM-LM). This holds in both warming scenarios, irrespective of whether the area increases or decreases. We hypothesize that models simulating a decrease in gyre area together with an increase in strength undergo a temporary spin-up as the gyre shrinks, as observed by Morison et al. (2021) in 2004–2019.

The remaining other 8 models exhibit a different behavior. Six of them simulate a decrease in strength in both scenarios, even for members without gyre disappearance in SSP2-4.5. This is the case for CMCC-ESM2, CNRM-CM6-1, CNRM-CM6-1-HR, CanESM5, IPSL-CM6A-LR, and MRI-ESM2-0 (Figure 4b). We note that all these models project particularly large area declines, with a complete gyre disappearance from all their members in SSP5-8.5. The other two models, the MPI model family, stand out with little notable changes in gyre strength, as for the area.

Table 2
Across-Model Correlation Between Temporal Changes in Beaufort Gyre (BG) Area or Strength, and for the Same SSP Scenario, Temporal Changes in SLP Mean, SLP Max, Beaufort High (BH) Index, Sea Ice Volume Mean, Sea Ice Area Mean, and Maximum Sea Ice Thickness

	SSP2-4.5 minus historical		SSP5-8.5 minus historical	
	BG area	BG strength	BG area	BG strength
SLP mean	0.28	0.24	**0.34**	0.25
SLP max	0.24	0.25	**0.35**	0.28
BH index	**0.33**	0.27	**0.41**	0.28
Sea ice area mean	**0.42**	0.09	**0.52**	0.3
Sea ice volume mean	−0.02	**−0.48**	0.04	−0.26
Sea ice thickness max	0.08	**−0.4**	0.12	−0.18

Note. All quantities are calculated over the BGx box. Temporal changes are computed as the difference between the 2070–2099 mean (for each SSP scenario) and the 1985–2014 mean (for the historical period). Significance at 95% is marked by bold font.

Finally, the CMIP6 simulations show a clear change in the location of the BG center, for projected months in which the gyre has not disappeared (Figures 4c and 4d). There is a stark southeastward shift of the gyre center in both warming scenarios, although no change is detected in the position of the BH. The shift is particularly striking in multimodel distributions and significant at the 99.99% confidence level. In other words, the simulated gyre centers retreat from a mostly central Canada Basin position in historical runs, to a location near the continental shelf of the Canadian mainland and archipelago toward the end of the century. This is reminiscent of the future Arctic sea ice distribution, historically accumulating north of the Canadian Archipelago and Greenland and similarly projected to be maintained latest in this region (Kwok, 2018; Selivanova et al., 2024). Very few models diverge from this archipelago-ward gyre shift. One model, INM-CM5-0, shows a northward shift coherent with its area increase (Figure 4c), and only three models comprise outlier members showing a westward displacement (Figure 4d).

3.3. Drivers of Future Beaufort Gyre Changes

Two mechanisms have been discussed in previous observation-based literature as the main possible drivers of future BG changes, with potentially opposing effects (see Section 1):

1. In the same way that intensified BH winds have driven the expansion of the BG in recent decades, a future reduction of the BH could weaken the gyre by decreasing anticyclonic wind stress (Kenigson & Timmermans, 2021; Proshutinsky et al., 2009; Regan et al., 2019).
2. Sea ice loss and thinning may induce a strengthened BG via increased wind energy input and stabilization by eddies (e.g., Armitage et al., 2020).

We first investigate whether these two mechanisms emerge in the CMIP6 simulations of long-term BG changes. Long-term changes are derived as the difference between the climatological means for the historical period (1985–2014) and for both SSP scenarios (2070–2099), as presented in Section 3.2 and introduced in the Methods. As expected, all considered CMIP6 models project a decrease in SLP and a decline in sea ice area, thickness, and volume in the Arctic Beaufort Sea (Figures S1 and S3 in Supporting Information S1). We calculate the across-model correlation between the amplitudes of such long-term reductions in BG area against those in sea ice area and SLP within the BGx box (black box in Figure 1). The first observation-based assumption is reproduced by the models: CMIP6 models with a stronger decrease in SLP tend to also have a stronger decrease in BG area, with an across-model correlation of 0.28 (nonsignificant) for SSP2-4.5 and 0.34 (significant at 95% level) for SSP5-8.5 (Table 2). The relationship is confirmed when excluding the outliers ACCESS-CM2 and INM-CM5-0, the only two models projecting a clear BG expansion: correlations increase to 0.49 and 0.51 respectively, and are highly significant. As the mean and maximum SLP in the BGx box does not necessarily represent the strength of the BH (M. Zhang et al., 2024), we note that these metrics could also reflect an Arctic-wide SLP decrease rather than changes specific to the BH. To better capture its strength, we additionally calculate a BH index (BH index), defined as the SLP difference between the BGx box and the surrounding Arctic region (≥66°N), excluding Greenland. Models that show a stronger reduction in this gradient also tend to have a stronger decrease in the BG area, with a significant across-model correlation of 0.33 for SSP2-4.5 and 0.41 for SSP5-8.5. The correlations increase to 0.58 and 0.57 when the two outlier models are excluded. Furthermore, we present the multimodel mean differences between the climatology of the scenario and the historical simulation in Figure S4 in Supporting Information S1, demonstrating that the strongest SLP decrease occurs in the area of the BH.

The second assumption, linking sea ice decline to a strengthening of the BG, is not, or only partly reproduced by the models. On the one hand, changes in BG strength exhibit an anticorrelation with the decline in sea ice volume and thickness (Table 2). This is consistent with the expected gyre strengthening under thinner ice conditions. On the other hand, we find that models with a stronger decrease in sea ice area tend to exhibit a stronger decrease in BG area, alongside a larger BH weakening (Figure S5 in Supporting Information S1). This high and significant correlation between the amplitude of sea ice and gyre area reductions in CMIP6 (Table 2) likely reflects their cooccurrence in response to the future Arctic warming, rather than a direct causality relation. While the future

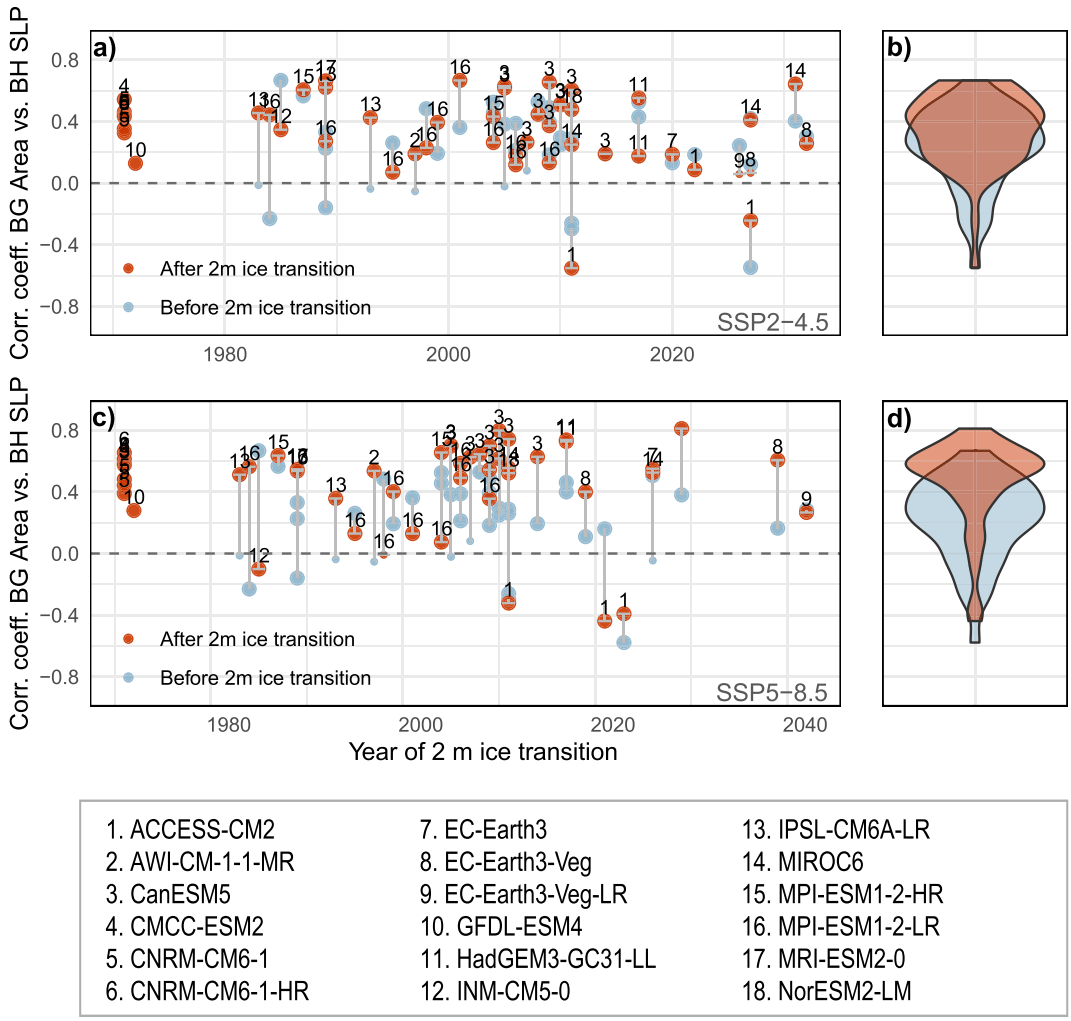

Figure 6. Correlation coefficients between the Beaufort Gyre area and the sea-level pressure in the BGx box (140°–230°E, 73°–90°N) for all selected models and their members, using historical runs combined with (a) SSP2-4.5 and (c) SSP5-8.5 projections. The associated density distributions are given in panel (b) for SSP2-4.5 and (d) for SSP5-8.5. Time series are split into two periods: one before the 2-m sea ice thickness transition to lower thicknesses (light blue) and one after the transition (dark red). The coefficients are sorted by years of transition on the *x*-axis. Four models (CMCC-ESM2, both CNRM models, and GFDL-ESM4) have already transitioned to a thin-ice Arctic as early as the early 1970s: due to the limited period, such time slices shorter than 5 years were excluded from correlation computations. The two correlation coefficient values (one for each time slice) for each member are connected by a gray line. Nonsignificant correlations are in smaller dots. CMIP6 models are indicated by a number.

thin-ice conditions may indeed increase wind stress, this effect is thus largely counterbalanced by the greater influence of the weakened BH in driving the simulated BG strength and area.

Indeed, the influence of the BH on gyre variations significantly increases after the transition to a thin-ice Arctic (Figure 6). We define the ice transition as the shift from a previously larger volume of thick ice to a predominance of ice thinner than 2 m (see Methods, Figure S1 in Supporting Information S1), named "2-m ice transition" hereafter. Most models transition to these thinner sea ice conditions between 1980 and 2020, indicating little dependency on the future emission scenario (Figures 6a and 6c). The large majority of models and members exhibit significant temporal correlations between monthly variations of the BG area and those of the superimposed SLP anomalies, and this relationship notably intensifies after the 2-m ice transition. As some if not most CMIP6 models are parametrized to modulate air-sea momentum fluxes based on sea ice cover rather than thickness (Martin et al., 2014), we repeated the analyses using SIC-based transition dates and obtained similar results. Here, we present the results derived from the physically more plausible SIT-based transition dates.

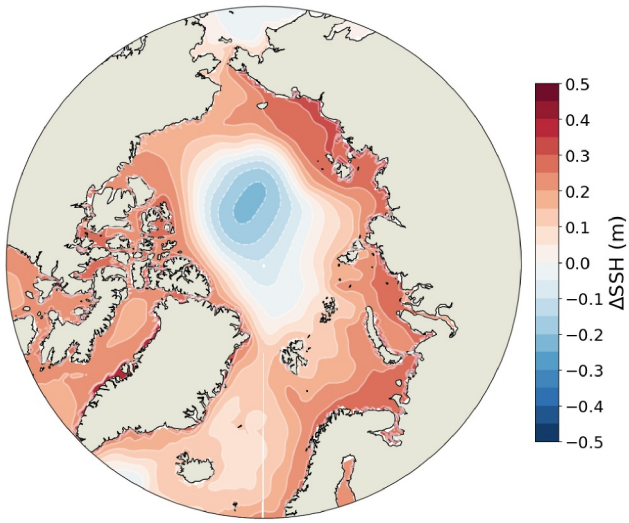

Figure 7. Projected SSH changes (m) between the 1985–2014 historical period and the 2070–2099 period at the end of the SSP5-8.5 scenario (30-year averages, see Methods), averaged over the models simulating a disappearance of the Beaufort Gyre (10 out of 18 models, with all their members).

The increase in correlation between the monthly BG area and SLP anomalies is particularly prominent in the multimodel distributions (Figures 6b and 6d), with a shift significant at the 95% confidence level for SSP2-4.5% and 99% for SSP5-8.5. Only 2 (4) out of 50 simulations exhibit an anticorrelation after the 2-m ice transition in SSP2-4.5 (SSP5-8.5). This unexpected anti-correlation is only present in ensemble members of ACCESS-CM2 and INM-CM5-0, which are the only two models that simulate an increase in the BG area under the two warming scenarios (see Section 3.2). Moreover, ACCESS-CM2 strongly overestimates the strength of the BH in the historical experiment (cf. Figure 2). When excluding these two models, 86% of the simulations feature an increase in correlations after the 2-m ice transition in SSP5-8.5 (59% in SSP2-4.5). This analysis was repeated using the earlier defined BH index instead of the mean SLP in the BGx box (Figure S6 in Supporting Information S1). The main results stay largely unchanged, indicating the robustness of the relationship.

In light of this relationship between SLP, sea ice cover, and the BG, it comes as no surprise that most models simulate a future reduction of the BG, as all analyzed CMIP6 models project a clear future weakening of the BH and transition to an atmosphere-dominated, thin-ice regime no later than 2040 (Figures S1 and S3 in Supporting Information S1).

3.4. Pan-Arctic Impacts of Beaufort Gyre Changes

Having demonstrated the interplay between changing atmospheric and sea ice forcing on the BG, we investigate the consequences of gyre changes for the pan-Arctic region. One obvious implication of a future BG decline, as projected by most CMIP6 models, is a broad change in SSH patterns. In the possible case of a disappearance of the BG, the SSH strongly decreases in the central Canadian Arctic, where most models simulate the historical gyre, while water volume is redistributed along the continental margins (Figure 7). However, in reality, the BG is more localized within the Beaufort Sea: with a more accurate representation of the gyre location, the SSH decline would likely be most pronounced in the Beaufort Sea rather than the central Arctic. This future increased contrast between shelves and the central Arctic would be in opposition with the SSH doming observed in 2003–2014 by Regan et al. (2019) (i.e., at the end of the historical period). Such a reshaping of future SSH gradients could have important implications for surface geostrophic currents in the Arctic, potentially favoring a more cyclonic large-scale flow, although multiple factors influence Arctic Ocean surface currents (Armitage et al., 2017, 2018; Timmermans & Marshall, 2020).

Table 3
Across-Model Correlation (Significant at 95%) Between Temporal Changes in Beaufort Gyre (BG) Area or Strength, and for the Same SSP Scenario, Temporal Changes in BG Salinity in the Halocline, in BG Stratification Approximated as Salinity Below the Halocline Minus That of the Halocline (See Methods), and in Salinity Difference in the Halocline Between Fram Strait or Davis Strait and the BG

	SSP2-4.5 minus historical		SSP5-8.5 minus historical	
	BG area	BG strength	BG area	BG strength
BG halocline salinity	−0.49	−0.82	−0.48	−0.53
BG stratification	0.61	0.67	0.70	0.59
Fram Strait minus BG	0.43	0.45	0.48	0.67
Davis Strait minus BG	0.48	0.63	0.46	0.49

Note. Temporal changes are computed as the difference between the 2070–2099 mean (for each SSP scenario) and the 1985–2014 mean (for the historical period). See also Figure 8.

Furthermore, as the BG is responsible for accumulating freshwater in the Arctic (see Section 1) we hypothesize that a decrease in BG area and/or strength under the warming scenarios would result in

1. a decrease in the freshwater content of the BG region or, in our case, an increase in salinity in the gyre halocline;
2. a decrease in the stratification in the BG region or, in our case, a decrease in the salinity difference between below and within the halocline; and
3. a decrease in the salinity difference between the BG region and the freshwater outflow regions, Fram and Davis straits.

We indeed find significant across-model correlations for all three hypotheses, for both SSP scenarios, when employing the models' ensemble mean (Table 3 and Figure 8) as well as the individual ensemble members (not shown). For clarity, we discuss correlations obtained from the ensemble means hereafter. Note also that although correlations are stronger when considering the BG strength changes rather than area changes (Table 3); this is most likely because the number of models is lower as the strength is meaningless when the gyre disappears. We therefore focus our analysis on the area changes (Figure 8).

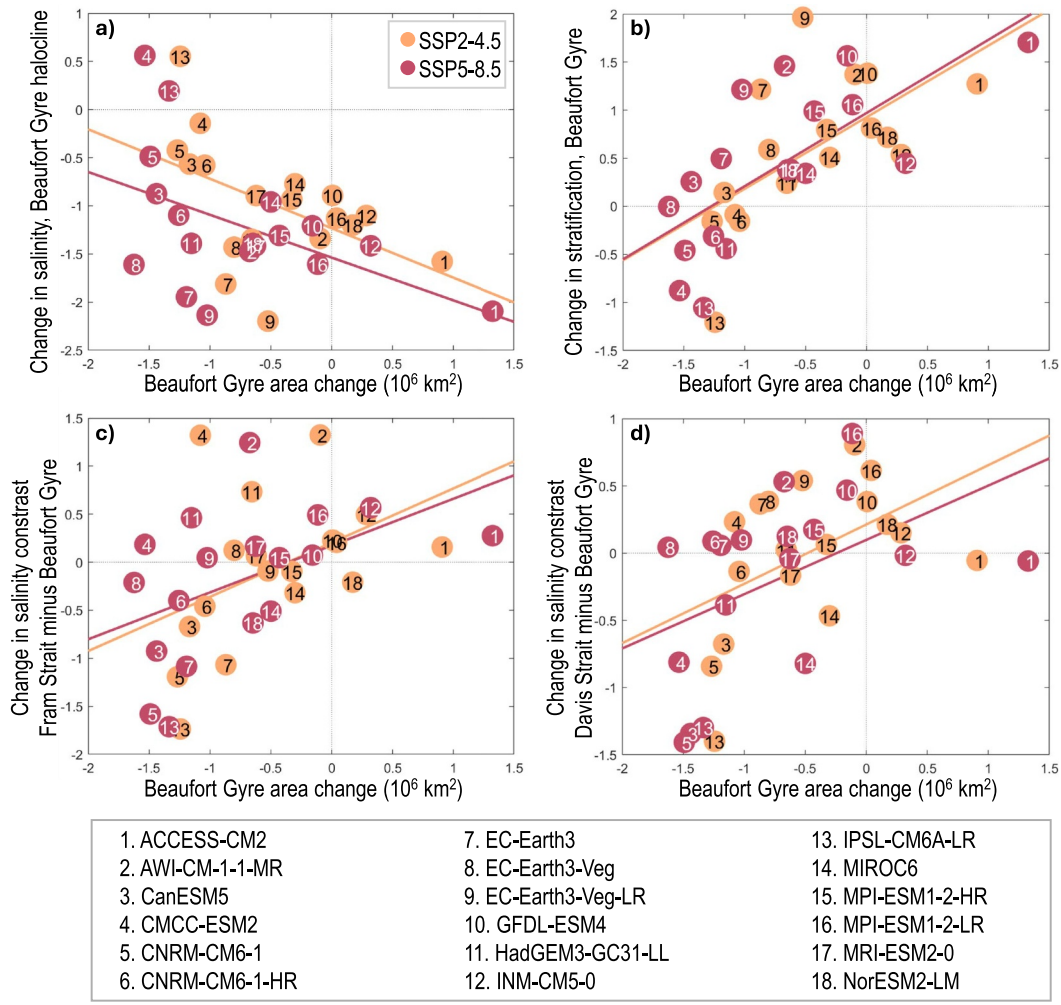

Figure 8. Across-model long-term changes in Beaufort Gyre (BG) area compared to changes in (a) the salinity of the halocline averaged within the BG; (b) the difference in salinity between below and within the halocline in the BG, proxy for stratification (see Method); (c) the upper-ocean salinity contrast between Fram Strait and the BG; and (d) the upper-ocean salinity contrast between Davis Strait and the BG. Long-term changes are computed as the difference between the 2070–2099 mean (for each SSP scenario) and the 1985–2014 mean (for the historical period). Colored lines are the linear regression lines for each SSP scenario. Correlation coefficients are reported in Table 3. All salinities are the models' practical salinity (unitless).

Salinity and area are anticorrelated, as expected: the weaker the BG becomes, the less freshwater remains accumulated in the region, that is, the saltier it becomes (Figure 8a). CanESM5, CNRM-CM6-1, the three EC-Earth3 models, HadGEM3-GC31-LL, and MRI-ESM2-0 are strong outliers, having seemingly a large freshening despite a large area decrease. As described in Section 3.2, these models exhibit a disappearance of their BG early in the warming scenario runs. The average over 2070–2100 therefore reflects changes after several decades without a gyre, that is, most likely not related to these models losing their gyre but rather to the superimposed freshening trend expected in a warmer Arctic (IPCC, 2019).

Some of these models are also obvious outliers when considering stratification changes (Figure 8b). The correlation between BG area and stratification, or strength of the halocline, is strongly significant and positive (Table 3): the weaker the gyre becomes, the less of a salinity difference between the halocline and below. There are fewer strong outliers, among which the EC-Earth3 models and MRI-ESM2-0 again, but also AWI-CM-1-1-MR, which features a particularly large and elongated gyre, and the nearly pan-Arctic MPI-ESM1-2-HR described in Section 3.1. AWI-CM-1-1-MR was not studied by Muilwijk et al. (2023), but they found that MPI-ESM1-2-HR was too weakly stratified throughout the Arctic and especially so in the Beaufort Sea in the

historical run. It is then not surprising that a model with an inaccurate BG shape and an inaccurate historical stratification also has a counterintuitive change in stratification.

Finally, changes in the BG area are positively correlated across models with changes in the upper-ocean salinity contrast between Fram (Figure 8c) or Davis (Figure 8d) straits and the BG region: when the BG weakens, so does the salinity contrast between these regions. We find again as strong outliers two to three models for which the BG disappears or is represented too elongated (AWI-CM-1-1-MR, CMCC-ESM2, and HadGEM3-GC31-LL for Fram Strait and AWI-CM-1-1-MR and the three EC-Earth3 models for Davis Strait). For both straits, we found no relationship between the change in salinity contrast and the change in the location of the center of the gyre (not shown). This is most likely because with so many models having no BG left, the concept of center of the gyre becomes meaningless. Another explanation could be that because the flow through each gateway is highly intermittent (Bertosio et al., 2022), our 30-year averages cannot detect correlations.

For all panels of Figure 8, outliers display large differences between the two scenario runs. These reflect the different times at which the models lose their BG, or the fact that they may lose it in one run and not in the other, as described in Section 3.2. For the models that align with the expected correlation, in general, the stronger the warming scenario, the stronger the change in both parameters in either direction.

In summary, as expected from the literature, CMIP6 models project that a decrease in BG area and strength is associated with an increased upper-ocean salinity and decreased stratification in the Beaufort Sea, as well as a decreased upper-ocean salinity contrast between the BG region and the freshwater exit gateways of Fram and Davis straits. That is, the BG region no longer accumulates freshwater.

4. Discussion and Concluding Remarks

We find here that a BG is represented by most CMIP6 models in the historical simulations. However, the gyre simulated by the 27 analyzed CMIP6 models is typically too strong, too large, and overly northward extended. Although most models simulate reasonably well the BH, the primary driver of the gyre, the unrealistic reproduction of BG characteristics by most CMIP6 models plausibly results from large biases that remain in the representation of Arctic sea ice and ocean properties, identified in previous studies (e.g., Muilwijk et al., 2023; Notz & SIMIP Community, 2020; S. Wang et al., 2022; Zanowski et al., 2021) and confirmed here.

In the second part of the study, we show that among the selected least unrealistic 18 models, most project a decline or disappearance of the BG by the end of the century, particularly for the high-emission scenario SSP5-8.5. We demonstrate that the simulated gyre decline is driven by a projected weakening of the BH, whose influence on the BG variations is enhanced by the transition to a thin-ice Arctic. These findings may seem contradictory at first with previous work suggesting that the declining Arctic sea ice could lead to a more energetic upper ocean (Armitage et al., 2020). In the CMIP6 models, we argue that the increased wind stress from sea ice thinning is likely largely offset by the stronger role of the weakened BH in regulating the BG strength and area. We further note that the previously suggested future spin-up of Arctic Ocean currents is not necessarily incompatible with a decline or disappearance of the BG, as the gyre strongly depends on the large-scale anticyclonic (clockwise) wind forcing. High-resolution results suggest that the projected enhanced mesoscale activity may be most prominent along continental slopes (Li et al., 2024). Using CMIP6 projections, Muilwijk et al. (2024) find a future weakening of the Beaufort Ekman pumping in the fall season when the gyre is climatologically at its seasonal peak: this would be in agreement with a possible gyre decline despite a generally more energetic Arctic. Finally, we show that the decline or disappearance of the gyre is associated with a redistribution of water volume along the continental margins, possibly reshaping large-scale surface currents in the Arctic. This coincides with a reduction of freshwater storage in the gyre, as well as salinity contrasts between the gyre surface, deeper levels, and freshwater outflows. This is in agreement with recent satellite observations, which indicate that water previously accumulated in the gyre area is now transiting toward Greenland and the Fram Strait (Q. Wang et al., 2024). Extended time series will be required to determine whether this behavior reflects natural variability, or marks the onset of the gyre decline projected in CMIP6 models.

Future changes in the strength and size of the BG could have important implications in the Arctic and beyond. Water volume redistribution may induce large changes in broad circulation patterns such as the BG and Transpolar Drift: this could in turn affect the distribution of nutrients and biogeochemical matter in the central

Arctic Ocean, as suggested by previous literature (Athanase et al., 2019; Boles et al., 2020; Krumpen et al., 2020; Zhuang et al., 2018). Further, the BG decline or disappearance would lead to a salinification and thus weakening of the halocline in the Beaufort Sea; in contrast, the associated release of freshwater from a weakened BG into the Arctic marginal seas and the North Atlantic would result in a local freshening and stronger upper-ocean stratification, thereby possibly hindering deep convection in these regions (D. S. Dukhovskoy et al., 2004; Heuzé & Liu, 2024; Proshutinsky et al., 2002). A potential subsequent reduction in deep water formation in the Nordic Seas could contribute to a slowdown or a northward shift of the Atlantic-Arctic meridional overturning circulation.

Despite a strong agreement of the projected changes across the models, it is worth bearing in mind that CMIP6 models lack important processes for the complex interaction between atmospheric drivers, the sea ice, and the upper ocean. As summarized by Doddridge et al. (2019), the air-ice-ocean couplings involve several processes that act at different timescales. Two of the main processes, namely the so-called "Ice-Ocean Governor" (relationship between ocean surface currents and the ice-ocean momentum transfer) and eddy diffusivity, are already included in CMIP models (see Doddridge et al., 2019, and references therein). Yet Manucharyan and Spall (2016) demonstrated that mesoscale eddies also play an important role in stabilizing the BG by laterally dissipating energy and thereby counterbalancing the air-sea momentum transfer. Doddridge et al. (2019) further showed that adding a mesoscale eddy parameterization to the simulated Ice Governor-eddy diffusivity balance dramatically improved the representation of the BG variability. Such a parameterization is not yet included in coarse-resolution CMIP6 models; therefore, their projections of the BG may need to be taken with caution. We additionally point out that the two drivers of the BG are linked, as atmospheric circulation changes influence the sea ice and vice versa. For instance, the positive phase of the Arctic oscillation is connected to below-average SLP in the Arctic, and at the same time, a winter sea ice thinning (Rigor et al., 2002), followed by reduced regional sea ice concentrations in summer (e.g., Gregory et al., 2022). The inaccurate representation of sea ice in CMIP6 models despite a relatively realistic representation of the BG could therefore suggest that the models may not correctly reproduce processes of atmosphere-ice coupling in the Arctic.

Nevertheless, this study provides the first comprehensive analyses of the Arctic BG in CMIP6 models and the potential future evolution of the gyre. All models agree on a future weakening of the BH, and therefore, the majority of the models also project a decline or disappearance of the BG. We show that the disappearance of the Gyre is most likely under the strongest emission scenario, whereas the gyre stabilizes in the middle-of-the-road simulation. This study therefore adds to the large body of literature as reviewed in IPCC (2019) that emphasizes that every fraction of a degree matters to prevent major changes to the Arctic and global climate system.

Data Availability Statement

CMIP6 model data are openly available via the Earth Grid System Federation. The DOIs and references of all the simulations we used are listed in Table S1 in Supporting Information S1; all outputs were last accessed on 11 August 2024. Here, we used the German Climate Computing center (DKRZ) node: https://esgf-data.dkrz.de/search/cmip6-dkrz/. Arctic bathymetry data are from the GEBCO Compilation Group, (2023), and can be retrieved at https://www.gebco.net. We used the ERA5 reanalysis data (Hersbach et al., 2020) made available at DKRZ, which are freely available online via the Copernicus Climate Data Store: https://cds.climate.copernicus.eu.

Acknowledgments
We acknowledge the World Climate Research Programme, which, through its Working Group on Coupled Modeling, coordinated and promoted CMIP6. We thank the climate modeling groups for producing and making available their model output, the ESGF for archiving the data and providing access, and the multiple funding agencies that support CMIP6 and ESGF. This work was first conceptualized during the workshop "Arctic Processes in CMIP6," organized by the CLIVAR/CliC Northern Oceans Region Panel. Marylou Athanase is supported by funding from the Climate Dynamics section of the Alfred Wegener Institute. Raphael Köhler is funded by the European Union's Horizon 2020 research and innovation framework programme under grant agreement 101003590 (PolarRES). Céline Heuzé is funded by a Swedish Research Council Starting Grant (dnr 2018-03859). We thank Ron Kwok for providing us with the SIT data used in Kwok (2018), and Heather Regan for providing the satellite-derived time series of gyre metrics used in Regan et al. (2019). Finally, we thank the associate editor and the three anonymous reviewers for their comments, which helped improve the manuscript. Open Access funding enabled and organized by Projekt DEAL.

References

Aagaard, K., & Carmack, E. C. (1989). The role of sea ice and other fresh water in the arctic circulation. *Journal of Geophysical Research*, *94*(C10), 14485–14498. https://doi.org/10.1029/JC094iC10p14485

Armitage, T. W. K., Bacon, S., & Kwok, R. (2018). Arctic sea level and surface circulation response to the arctic oscillation. *Geophysical Research Letters*, *45*(13), 6576–6584. https://doi.org/10.1029/2018GL078386

Armitage, T. W. K., Bacon, S., Ridout, A. L., Petty, A. A., Wolbach, S., & Tsamados, M. (2017). Arctic ocean surface geostrophic circulation 2003–2014. *The Cryosphere*, *11*(4), 1767–1780. https://doi.org/10.5194/tc-11-1767-2017

Armitage, T. W. K., Manucharyan, G. E., Petty, A. A., Kwok, R., & Thompson, A. F. (2020). Enhanced eddy activity in the Beaufort Gyre in response to sea ice loss. *Nature Communications*, *11*(1), 761. https://doi.org/10.1038/s41467-020-14449-z

Athanase, M., Sennéchael, N., Garric, G., Koenig, Z., Boles, E., & Provost, C. (2019). New hydrographic measurements of the upper arctic western Eurasian basin in 2017 reveal fresher mixed layer and shallower warm layer than 2005–2012 climatology. *Journal of Geophysical Research: Oceans*, *124*(2), 1091–1114. https://doi.org/10.1029/2018JC014701

Bertosio, C., Provost, C., Athanase, M., Sennéchael, N., Garric, G., Lellouche, J. M., et al. (2022). Changes in freshwater distribution and pathways in the Arctic Ocean since 2007 in the Mercator Ocean global operational system. *Journal of Geophysical Research: Oceans*, *127*(6), e2021JC017701. https://doi.org/10.1029/2021JC017701

Boles, E., Provost, C., Garçon, V., Bertosio, C., Athanase, M., Koenig, Z., & Sennéchael, N. (2020). Under-ice phytoplankton blooms in the central Arctic Ocean: Insights from the first biogeochemical IAOOS platform drift in 2017. *Journal of Geophysical Research: Oceans*, *125*(3), e2019JC015608. https://doi.org/10.1029/2019JC015608

Cole, S. T., Toole, J. M., Lele, R., Timmermans, M.-L., Gallaher, S. G., Stanton, T. P., et al. (2017). Ice and ocean velocity in the arctic marginal ice zone: Ice roughness and momentum transfer. *Elem Sci Anth*, *5*, 55. https://doi.org/10.1525/elementa.241

Doddridge, E. W., Meneghello, G., Marshall, J., Scott, J., & Lique, C. (2019). A three-way balance in the Beaufort Gyre: The ice-ocean governor, wind stress, and eddy diffusivity. *Journal of Geophysical Research: Oceans*, *124*(5), 3107–3124. https://doi.org/10.1029/2018JC014897

Dukhovskoy, D., Johnson, M., & Proshutinsky, A. (2006). Arctic decadal variability from an idealized atmosphere-ice-ocean model: 2. Simulation of decadal oscillations. *Journal of Geophysical Research*, *111*(C6), C06029. https://doi.org/10.1029/2004JC002820

Dukhovskoy, D. S., Johnson, M. A., & Proshutinsky, A. (2004). Arctic decadal variability: An auto-oscillatory system of heat and fresh water exchange. *Geophysical Research Letters*, *31*(3), L03302. https://doi.org/10.1029/2003GL019023

Eyring, V., Bony, S., Meehl, G., Senior, C., Stevens, B., Stouffer, R., & Taylor, K. (2016). Overview of the coupled model intercomparison project phase 6 (CMIP6) experimental design and organization. *Geoscientific Model Development*, *9*(5), 1937–1958. https://doi.org/10.5194/gmd-9-1937-2016

GEBCO Compilation Group. (2023). *The gebco_2023 grid-a continuous terrain model of the global oceans and land*. nerc eds british oceanographic data centre noc. https://doi.org/10.5285/f98b053b-0cbc-6c23-e053-6c86abc0af7b

Gregory, W., Stroeve, J., & Tsamados, M. (2022). Network connectivity between the winter arctic oscillation and summer sea ice in cmip6 models and observations. *The Cryosphere*, *16*(5), 1653–1673. https://doi.org/10.5194/tc-16-1653-2022

Griffies, S., Danabasoglu, G., Durack, P., Adcroft, A., Balaji, V., Böning, C., et al. (2016). OMIP contribution to CMIP6: Experimental and diagnostic protocol for the physical component of the Ocean Model Intercomparison Project. *Geoscientific Model Development*, *9*, 3231–3296. https://doi.org/10.5194/gmd-9-3231-2016

Hersbach, H., Bell, B., Berrisford, P., Hirahara, S., Horányi, A., Muñoz-Sabater, J., et al. (2020). The ERA5 global reanalysis. *Quarterly Journal of the Royal Meteorological Society*, *146*(730), 1999–2049. https://doi.org/10.1002/qj.3803

Heuzé, C., & Liu, H. (2024). No emergence of deep convection in the Arctic Ocean across CMIP6 models. *Geophysical Research Letters*, *51*(4), e2023GL106499. https://doi.org/10.1029/2023GL106499

Heuzé, C., Zanowski, H., Karam, S., & Muilwijk, M. (2023). The deep Arctic Ocean and fram strait in CMIP6 models. *Journal of Climate*, *36*(8), 2551–2584. https://doi.org/10.1175/JCLI-D-22-0194.1

Hibler, W. D. III. (1979). A dynamic thermodynamic sea ice model. *Journal of Physical Oceanography*, *9*(4), 815–846. https://doi.org/10.1175/1520-0485(1979)009⟨0815:ADTSIM⟩2.0.CO;2

IPCC. (2019). H. Pörtner, et al. (Eds.) *IPCC special report on the ocean and cryosphere in a changing climate*. Cambridge University Press.

Karpechko, A. Y., Afargan-Gerstman, H., Butler, A. H., Domeisen, D. I., Kretschmer, M., Lawrence, Z., et al. (2022). Northern hemisphere stratosphere-troposphere circulation change in CMIP6 models: 1. Inter-model spread and scenario sensitivity. *Journal of Geophysical Research: Atmospheres*, *127*(18), e2022JD036992. https://doi.org/10.1029/2022JD036992

Kelly, S., Proshutinsky, A., Popova, E., Aksenov, Y., & Yool, A. (2019). On the origin of water masses in the Beaufort Gyre. *Journal of Geophysical Research: Oceans*, *124*(7), 4696–4709. https://doi.org/10.1029/2019JC015022

Kenigson, J. S., & Timmermans, M.-L. (2021). Arctic cyclone activity and the Beaufort High. *Journal of Climate*, *34*(10), 4119–4127. https://doi.org/10.1175/JCLI-D-20-0771.1

Khosravi, N., Wang, Q., Koldunov, N., Hinrichs, C., Semmler, T., Danilov, S., & Jung, T. (2022). The arctic ocean in CMIP6 models: Biases and projected changes in temperature and salinity. *Earth's Future*, *10*(2), e2021EF002282. https://doi.org/10.1029/2021EF002282

Krumpen, T., Birrien, F., Kauker, F., Rackow, T., Von Albedyll, L., Angelopoulos, M., et al. (2020). The mosaic ice floe: Sediment-laden survivor from the siberian shelf. *The Cryosphere*, *14*(7), 2173–2187. https://doi.org/10.5194/tc-14-2173-2020

Kwok, R. (2018). Arctic sea ice thickness, volume, and multiyear ice coverage: Losses and coupled variability (1958–2018). *Environmental Research Letters*, *13*(10), 105005. https://doi.org/10.1088/1748-9326/aae3ec

Lavergne, T., Sørensen, A. M., Kern, S., Tonboe, R., Notz, D., Aaboe, S., et al. (2019). Version 2 of the EUMETSAT OSI SAF and ESA CCI sea-ice concentration climate data records. *The Cryosphere*, *13*(1), 49–78. https://doi.org/10.5194/tc-13-49-2019

Li, X., Wang, Q., Danilov, S., Koldunov, N., Liu, C., Müller, V., et al. (2024). Eddy activity in the Arctic Ocean projected to surge in a warming world. *Nature Climate Change*, *14*(2), 156–162. https://doi.org/10.1038/s41558-023-01908-w

Mahoney, A. R., Hutchings, J. K., Eicken, H., & Haas, C. (2019). Changes in the thickness and circulation of multiyear ice in the Beaufort Gyre determined from pseudo-Lagrangian methods from 2003–2015. *Journal of Geophysical Research: Oceans*, *124*(8), 5618–5633. https://doi.org/10.1029/2018JC014911

Manucharyan, G. E., & Spall, M. A. (2016). Wind-driven freshwater buildup and release in the Beaufort Gyre constrained by mesoscale eddies. *Geophysical Research Letters*, *43*(1), 273–282. https://doi.org/10.1002/2015GL065957

Manucharyan, G. E., & Thompson, A. F. (2022). Heavy footprints of upper-ocean eddies on weakened arctic sea ice in marginal ice zones. *Nature Communications*, *13*(1), 2147. https://doi.org/10.1038/s41467-022-29663-0

Martin, T., Steele, M., & Zhang, J. (2014). Seasonality and long-term trend of arctic ocean surface stress in a model. *Journal of Geophysical Research: Oceans*, *119*(3), 1723–1738. https://doi.org/10.1002/2013JC009425

Meinshausen, M., Nicholls, Z. R., Lewis, J., Gidden, M. J., Vogel, E., Freund, M., et al. (2020). The shared socio-economic pathway (SSP) greenhouse gas concentrations and their extensions to 2500. *Geoscientific Model Development*, *13*(8), 3571–3605. https://doi.org/10.5194/gmd-13-3571-2020

Moore, G., Schweiger, A., Zhang, J., & Steele, M. (2018). Collapse of the 2017 winter Beaufort High: A response to thinning sea ice? *Geophysical Research Letters*, *45*(6), 2860–2869. https://doi.org/10.1002/2017GL076446

Morison, J., Kwok, R., Dickinson, S., Andersen, R., Peralta-Ferriz, C., Morison, D., et al. (2021). The cyclonic mode of arctic ocean circulation. *Journal of Physical Oceanography*, *51*(4), 1053–1075. https://doi.org/10.1175/JPO-D-20-0190.1

Muilwijk, M., Hattermann, T., Martin, T., & Granskog, M. A. (2024). Future sea ice weakening amplifies wind-driven trends in surface stress and arctic ocean spin-up. *Nature Communications*, *15*(1), 6889. https://doi.org/10.1038/s41467-024-50874-0

Muilwijk, M., Nummelin, A., Heuzé, C., Polyakov, I., Zanowski, H., & Smedsrud, L. (2023). Divergence in climate model projections of future Arctic Atlantification. *Journal of Climate*, *36*(6), 1727–1748. https://doi.org/10.1175/JCLI-D-22-0349.1

Notz, D., & Community, S. (2020). Arctic sea ice in cmip6. *Geophysical Research Letters*, *47*(10), e2019GL086749. https://doi.org/10.1029/2019GL086749

O'Neill, B., Tebaldi, C., Van Vuuren, D., Eyring, V., Friedlingstein, P., Hurtt, G., et al. (2016). The scenario model intercomparison project (ScenarioMIP) for CMIP6. *Geoscientific Model Development*, *9*, 3461–3482. https://doi.org/10.5194/gmd-9-3461-2016

Polyakov, I. V., Pnyushkov, A. V., & Carmack, E. C. (2018). Stability of the arctic halocline: A new indicator of arctic climate change. *Environmental Research Letters*, *13*(12), 125008. https://doi.org/10.1088/1748-9326/aaec1e

Proshutinsky, A., Bourke, R., & McLaughlin, F. (2002). The role of the Beaufort Gyre in Arctic climate variability: Seasonal to decadal climate scales. *Geophysical Research Letters*, *29*(23), 2100. https://doi.org/10.1029/2002GL015847

Proshutinsky, A., Dukhovskoy, D., Timmermans, M.-L., Krishfield, R., & Bamber, J. L. (2015). Arctic circulation regimes. *Philosophical Transactions of the Royal Society A: Mathematical, Physical & Engineering Sciences*, *373*(2052), 20140160. https://doi.org/10.1098/rsta.2014.0160

Proshutinsky, A., & Johnson, M. A. (1997). Two circulation regimes of the wind-driven arctic ocean. *Journal of Geophysical Research*, *102*(C6), 12493–12514. https://doi.org/10.1029/97JC00738

Proshutinsky, A., Krishfield, R., Timmermans, M.-L., Toole, J., Carmack, E., McLaughlin, F., et al. (2009). Beaufort Gyre freshwater reservoir: State and variability from observations. *Journal of Geophysical Research*, *114*(C1). https://doi.org/10.1029/2008JC005104

Proshutinsky, A., Krishfield, R., Toole, J., Timmermans, M.-L., Williams, W., Zimmermann, S., et al. (2019). Analysis of the Beaufort Gyre freshwater content in 2003–2018. *Journal of Geophysical Research: Oceans*, *124*(12), 9658–9689. https://doi.org/10.1029/2019JC015281

Rabe, B., Karcher, M., Schauer, U., Toole, J. M., Krishfield, R. A., Pisarev, S., et al. (2011). An assessment of arctic ocean freshwater content changes from the 1990s to the 2006–2008 period. *Deep Sea Research Part I: Oceanographic Research Papers*, *58*(2), 173–185. https://doi.org/10.1016/j.dsr.2010.12.002

Regan, H. C., Lique, C., & Armitage, T. W. K. (2019). The Beaufort Gyre extent, shape, and location between 2003 and 2014 from satellite observations. *Journal of Geophysical Research: Oceans*, *124*(2), 844–862. https://doi.org/10.1029/2018JC014379

Rigor, I. G., Wallace, J. M., & Colony, R. L. (2002). Response of sea ice to the arctic oscillation. *Journal of Climate*, *15*(18), 2648–2663. https://doi.org/10.1175/1520-0442(2002)015⟨2648:ROSITT⟩2.0.CO;2

Rudels, B., Jones, E. P., Schauer, U., & Eriksson, P. (2004). Atlantic sources of the arctic ocean surface and halocline waters. *Polar Research*, *23*(2), 181–208. https://doi.org/10.3402/polar.v23i2.6278

Schauer, U., & Losch, M. (2019). "Freshwater" in the ocean is not a useful parameter in climate research. *Journal of Physical Oceanography*, *49*(9), 2309–2321. https://doi.org/10.1175/JPO-D-19-0102.1

Selivanova, J., Iovino, D., & Cocetta, F. (2024). Past and future of the arctic sea ice in high-resolution model intercomparison project (highresmip) climate models. *The Cryosphere*, *18*(6), 2739–2763. https://doi.org/10.5194/tc-18-2739-2024

Semmler, T., Danilov, S., Gierz, P., Goessling, H., Hegewald, J., Hinrichs, C., et al. (2020). Simulations for CMIP6 with the AWI climate model AWI-CM-1-1. *Journal of Advances in Modeling Earth Systems*, *12*(9), e2019MS002009. https://doi.org/10.1029/2019MS002009

Serreze, M. C., & Barrett, A. P. (2011). Characteristics of the Beaufort Sea high. *Journal of Climate*, *24*(1), 159–182. https://doi.org/10.1175/2010JCLI3636.1

Shu, Q., Wang, Q., Årthun, M., Wang, S., Song, Z., Zhang, M., & Qiao, F. (2022). Arctic Ocean Amplification in a warming climate in CMIP6 models. *Science Advances*, *8*(30), eabn9755. https://doi.org/10.1126/sciadv.abn9755

Smith, D. M., Eade, R., Andrews, M., Ayres, H., Clark, A., Chripko, S., et al. (2022). Robust but weak winter atmospheric circulation response to future arctic sea ice loss. *Nature Communications*, *13*(1), 727. https://doi.org/10.1038/s41467-022-28283-y

Solomon, A., Heuzé, C., Rabe, B., Bacon, S., Bertino, L., Heimbach, P., et al. (2021). Freshwater in the Arctic Ocean 2010–2019. *Ocean Science*, *17*(4), 1081–1102. https://doi.org/10.5194/os-17-1081-2021

Song, J.-N., Fu, G., Xu, Y., Han, Z.-Y., Sun, Q.-Z., & Wang, H. (2021). Assessment of the capability of cmip6 global climate models to simulate arctic cyclones. *Advances in Climate Change Research*, *12*(5), 660–676. https://doi.org/10.1016/j.accre.2021.07.007

Timmermans, M.-L., & Marshall, J. (2020). Understanding Arctic Ocean circulation: A review of ocean dynamics in a changing climate. *Journal of Geophysical Research: Oceans*, *125*(4), e2018JC014378. https://doi.org/10.1029/2018JC014378

Timmermans, M.-L., & Toole, J. (2023). The Arctic Ocean's Beaufort Gyre. *Annual Review of Marine Science*, *15*(1), 223–248. https://doi.org/10.1146/annurev-marine-032122-012034

Vellinga, M., Dickson, B., & Curry, R. (2008). The changing view on how freshwater impacts the Atlantic meridional overturning circulation. In *Arctic–subarctic ocean fluxes: Defining the role of the northern seas in climate* (pp. 289–313). Springer. https://doi.org/10.1007/978-1-4020-6774-7_13

Wang, Q., Danilov, S., & Jung, T. (2024). Arctic freshwater anomaly transiting to the north atlantic delayed within a buffer zone. *Nature Geoscience*, *17*(12), 1–4. https://doi.org/10.1038/s41561-024-01592-1

Wang, S., Wang, Q., Wang, M., Lohmann, G., & Qiao, F. (2022). Arctic ocean freshwater in cmip6 coupled models. *Earth's Future*, *10*(9), e2022EF002878. https://doi.org/10.1029/2022EF002878

Wang, X., Lu, R., Wang, S.-Y., Chen, R.-T., Chen, Z.-Q., Hui, F.-M., et al. (2023). Assessing cmip6 simulations of arctic sea ice drift: Role of near-surface wind and surface ocean current in model performance. *Advances in Climate Change Research*, *14*(5), 691–706. https://doi.org/10.1016/j.accre.2023.09.005

Zanowski, H., Jahn, A., & Holland, M. M. (2021). Arctic ocean freshwater in CMIP6 ensembles: Declining sea ice, increasing ocean storage and export. *Journal of Geophysical Research: Oceans*, *126*(4), e2020JC016930. https://doi.org/10.1029/2020JC016930

Zapponini, M., & Goessling, H. F. (2024). Atmospheric destabilization leads to Arctic Ocean winter surface wind intensification. *Communications Earth & Environment*, *5*(1), 262. https://doi.org/10.1038/s43247-024-01428-1

Zhang, J., Weijer, W., Steele, M., Cheng, W., Verma, T., & Veneziani, M. (2021). Labrador sea freshening linked to Beaufort Gyre freshwater release. *Nature Communications*, *12*(1), 1229. https://doi.org/10.1038/s41467-021-21470-3

Zhang, M., Perrie, W., & Long, Z. (2024). Future changes in the winter Beaufort High under warming climate scenarios. *Geophysical Research Letters*, *51*(16), e2024GL110317. https://doi.org/10.1029/2024GL110317

Zhao, B., & Timmermans, M.-L. (2018). Topographic rossby waves in the Arctic Ocean's Beaufort Gyre. *Journal of Geophysical Research: Oceans*, *123*(9), 6521–6530. https://doi.org/10.1029/2018JC014233

Zhuang, Y., Jin, H., Chen, J., Li, H., Ji, Z., Bai, Y., & Zhang, T. (2018). Nutrient and phytoplankton dynamics driven by the Beaufort Gyre in the western arctic ocean during the period 2008–2014. *Deep Sea Research Part I: Oceanographic Research Papers*, *137*, 30–37. https://doi.org/10.1016/j.dsr.2018.05.002

References From the Supporting Information

Bentsen, M., Oliviè, D. J. L., Seland, Ø., Toniazzo, T., Gjermundsen, A., Graff, L. S., et al. (2019). NCC NorESM2-MM model output prepared for CMIP6 CMIP historical [Dataset]. *Earth System Grid Federation*. https://doi.org/10.22033/ESGF/CMIP6.8040

Boucher, O., Denvil, S., Levavasseur, G., Cozic, A., Caubel, A., Foujols, M.-A., et al. (2018). IPSL IPSL-CM6A-LR model output prepared for CMIP6 CMIP historical [Dataset]. *Earth System Grid Federation*. https://doi.org/10.22033/ESGF/CMIP6.5195
Boucher, O., Denvil, S., Levavasseur, G., Cozic, A., Caubel, A., Foujols, M.-A., et al. (2019a). IPSL IPSL-CM6A-LR model output prepared for CMIP6 ScenarioMIP SSP245 [Dataset]. *Earth System Grid Federation*. https://doi.org/10.22033/ESGF/CMIP6.5264
Boucher, O., Denvil, S., Levavasseur, G., Cozic, A., Caubel, A., Foujols, M.-A., et al. (2019b). IPSL IPSL-CM6A-LR model output prepared for CMIP6 ScenarioMIP SSP585 [Dataset]. *Earth System Grid Federation*. https://doi.org/10.22033/ESGF/CMIP6.5271
Dix, M., Bi, D., Dobrohotoff, P., Fiedler, R., Harman, I., Law, R., et al. (2019a). CSIRO-ARCCSS ACCESS-CM2 model output prepared for CMIP6 CMIP historical [Dataset]. *Earth System Grid Federation*. https://doi.org/10.22033/ESGF/CMIP6.4271
Dix, M., Bi, D., Dobrohotoff, P., Fiedler, R., Harman, I., Law, R., et al. (2019b). CSIRO-ARCCSS ACCESS-CM2 model output prepared for CMIP6 ScenarioMIP ssp245 [Dataset]. *Earth System Grid Federation*. https://doi.org/10.22033/ESGF/CMIP6.4321
Dix, M., Bi, D., Dobrohotoff, P., Fiedler, R., Harman, I., Law, R., et al. (2019c). CSIRO-ARCCSS ACCESS-CM2 model output prepared for CMIP6 ScenarioMIP ssp585 [Dataset]. *Earth System Grid Federation*. https://doi.org/10.22033/ESGF/CMIP6.4332
EC-Earth Consortium (EC-Earth). (2019a). EC-Earth-Consortium EC-Earth3 model output prepared for CMIP6 CMIP historical [Dataset]. *Earth System Grid Federation*. https://doi.org/10.22033/ESGF/CMIP6.4700
EC-Earth Consortium (EC-Earth). (2019b). EC-Earth-Consortium EC-Earth3 model output prepared for CMIP6 ScenarioMIP SSP245 [Dataset]. *Earth System Grid Federation*. https://doi.org/10.22033/ESGF/CMIP6.4880
EC-Earth Consortium (EC-Earth). (2019c). EC-Earth-Consortium EC-Earth3 model output prepared for CMIP6 ScenarioMIP SSP585 [Dataset]. *Earth System Grid Federation*. https://doi.org/10.22033/ESGF/CMIP6.4912
EC-Earth Consortium (EC-Earth). (2019d). EC-Earth-Consortium EC-Earth3-Veg model output prepared for CMIP6 ScenarioMIP [Dataset]. *Earth System Grid Federation*. https://doi.org/10.22033/ESGF/CMIP6.727
EC-Earth Consortium (EC-Earth). (2019e). EC-Earth-Consortium EC-Earth3-Veg model output prepared for CMIP6 ScenarioMIP SSP245 [Dataset]. *Earth System Grid Federation*. https://doi.org/10.22033/ESGF/CMIP6.4882
EC-Earth Consortium (EC-Earth). (2019f). EC-Earth-Consortium EC-Earth3-Veg model output prepared for CMIP6 ScenarioMIP ssp585 [Dataset]. *Earth System Grid Federation*. https://doi.org/10.22033/ESGF/CMIP6.4914
EC-Earth Consortium (EC-Earth). (2020a). EC-Earth-Consortium EC-Earth3-Veg-LR model output prepared for CMIP6 CMIP historical [Dataset]. *Earth System Grid Federation*. https://doi.org/10.22033/ESGF/CMIP6.4707
EC-Earth Consortium (EC-Earth). (2020b). EC-Earth-Consortium EC-Earth3-Veg-LR model output prepared for CMIP6 ScenarioMIP ssp245 [Dataset]. *Earth System Grid Federation*. https://doi.org/10.22033/ESGF/CMIP6.4883
EC-Earth Consortium (EC-Earth). (2020c). EC-Earth-Consortium EC-Earth3-Veg-LR model output prepared for CMIP6 ScenarioMIP ssp585 [Dataset]. *Earth System Grid Federation*. https://doi.org/10.22033/ESGF/CMIP6.4915
EC-Earth Consortium (EC-Earth). (2021). EC-Earth-Consortium EC-Earth-3-CC model output prepared for CMIP6 CMIP historical [Dataset]. *Earth System Grid Federation*. https://doi.org/10.22033/ESGF/CMIP6.4702
Good, P. (2019). MOHC HadGEM3-GC31-LL model output prepared for CMIP6 ScenarioMIP SSP245 [Dataset]. *Earth System Grid Federation*. https://doi.org/10.22033/ESGF/CMIP6.10851
Good, P. (2020). MOHC HadGEM3-GC31-LL model output prepared for CMIP6 ScenarioMIP SSP585 [Dataset]. *Earth System Grid Federation*. https://doi.org/10.22033/ESGF/CMIP6.10901
Huang, W. (2019). THU CIESM model output prepared for CMIP6 CMIP historical [Dataset]. *Earth System Grid Federation*. https://doi.org/10.22033/ESGF/CMIP6.8843
John, J. G., Blanton, C., McHugh, C., Radhakrishnan, A., Rand, K., Vahlenkamp, H., et al. (2018a). NOAA-GFDL GFDL-ESM4 model output prepared for CMIP6 ScenarioMIP SSP245 [Dataset]. *Earth System Grid Federation*. https://doi.org/10.22033/ESGF/CMIP6.8686
John, J. G., Blanton, C., McHugh, C., Radhakrishnan, A., Rand, K., Vahlenkamp, H., et al. (2018b). NOAA-GFDL GFDL-ESM4 model output prepared for CMIP6 ScenarioMIP SSP585 [Dataset]. *Earth System Grid Federation*. https://doi.org/10.22033/ESGF/CMIP6.8706
Jungclaus, J., Bittner, M., Wieners, K.-H., Wachsmann, F., Schupfner, M., Legutke, S., et al. (2019). MPI-M MPI-ESM1.2-HR model output prepared for CMIP6 CMIP historical [Dataset]. *Earth System Grid Federation*. https://doi.org/10.22033/ESGF/CMIP6.6594
Krasting, J. P., John, J. G., Blanton, C., McHugh, C., Nikonov, S., Radhakrishnan, A., et al. (2018). NOAA-GFDL GFDL-ESM4 model output prepared for CMIP6 CMIP historical [Dataset]. *Earth System Grid Federation*. https://doi.org/10.22033/ESGF/CMIP6.8597
Lovato, T., & Peano, D. (2020). CMCC CMCC-CM2-SR5 model output prepared for CMIP6 CMIP historical [Dataset]. *Earth System Grid Federation*. https://doi.org/10.22033/ESGF/CMIP6.3825
Lovato, T., Peano, D., & Butenschön, M. (2021a). CMCC CMCC-ESM2 model output prepared for CMIP6 CMIP historical [Dataset]. *Earth System Grid Federation*. https://doi.org/10.22033/ESGF/CMIP6.13195
Lovato, T., Peano, D., & Butenschön, M. (2021b). CMCC CMCC-ESM2 model output prepared for CMIP6 ScenarioMIP ssp245 [Dataset]. *Earth System Grid Federation*. https://doi.org/10.22033/ESGF/CMIP6.13252
Lovato, T., Peano, D., & Butenschön, M. (2021c). CMCC CMCC-ESM2 model output prepared for CMIP6 ScenarioMIP ssp585 [Dataset]. *Earth System Grid Federation*. https://doi.org/10.22033/ESGF/CMIP6.13259
Ridley, J., Menary, M., Kuhlbrodt, T., Andrews, M., & Andrews, T. (2019). MOHC HadGEM3-GC31-LL model output prepared for CMIP6 CMIP historical [Dataset]. *Earth System Grid Federation*. https://doi.org/10.22033/ESGF/CMIP6.6109
Rong, X. (2019). CAMS CAMS_CSM1.0 model output prepared for CMIP6 CMIP historical [Dataset]. *Earth System Grid Federation*. https://doi.org/10.22033/ESGF/CMIP6.9754
Schupfner, M., Wieners, K.-H., Wachsmann, F., Steger, C., Bittner, M., Jungclaus, J., et al. (2019a). DKRZ MPI-ESM1.2-HR model output prepared for CMIP6 ScenarioMIP SSP245 [Dataset]. *Earth System Grid Federation*. https://doi.org/10.22033/ESGF/CMIP6.4398
Schupfner, M., Wieners, K.-H., Wachsmann, F., Steger, C., Bittner, M., Jungclaus, J., et al. (2019b). DKRZ MPI-ESM1.2-HR model output prepared for CMIP6 ScenarioMIP ssp585 [Dataset]. *Earth System Grid Federation*. https://doi.org/10.22033/ESGF/CMIP6.4403
Seland, Ø., Bentsen, M., Oliviè, D. J. L., Toniazzo, T., Gjermundsen, A., Graff, L. S., et al. (2019a). NCC NorESM2-LM model output prepared for CMIP6 CMIP historical [Dataset]. *Earth System Grid Federation*. https://doi.org/10.22033/ESGF/CMIP6.8036
Seland, Ø., Bentsen, M., Oliviè, D. J. L., Toniazzo, T., Gjermundsen, A., Graff, L. S., et al. (2019b). NCC NorESM2-LM model output prepared for CMIP6 ScenarioMIP SSP245 [Dataset]. *Earth System Grid Federation*. https://doi.org/10.22033/ESGF/CMIP6.8253
Seland, Ø., Bentsen, M., Oliviè, D. J. L., Toniazzo, T., Gjermundsen, A., Graff, L. S., et al. (2019c). NCC NorESM2-LM model output prepared for CMIP6 ScenarioMIP ssp585 [Dataset]. *Earth System Grid Federation*. https://doi.org/10.22033/ESGF/CMIP6.8319
Semmler, T., Danilov, S., Rackow, T., Sidorenko, D., Barbi, D., Hegewald, J., et al. (2018a). AWI AWI-CM1.1MR model output prepared for CMIP6 CMIP historical [Dataset]. *Earth System Grid Federation*. https://doi.org/10.22033/ESGF/CMIP6.2686
Semmler, T., Danilov, S., Rackow, T., Sidorenko, D., Barbi, D., Hegewald, J., et al. (2018b). AWI AWI-CM1.1MR model output prepared for CMIP6 ScenarioMIP SSP245 [Dataset]. *Earth System Grid Federation*. https://doi.org/10.22033/ESGF/CMIP6.2800

Semmler, T., Danilov, S., Rackow, T., Sidorenko, D., Barbi, D., Hegewald, J., et al. (2019). AWI AWI-CM1.1MR model output prepared for CMIP6 ScenarioMIP ssp585 [Dataset]. *Earth System Grid Federation*. https://doi.org/10.22033/ESGF/CMIP6.2817
Shiogama, H., Abe, M., & Tatebe, H. (2019a). MIROC MIROC6 model output prepared for CMIP6 ScenarioMIP SSP245 [Dataset]. *Earth System Grid Federation*. https://doi.org/10.22033/ESGF/CMIP6.5746
Shiogama, H., Abe, M., & Tatebe, H. (2019b). MIROC MIROC6 model output prepared for CMIP6 ScenarioMIP ssp585 [Dataset]. *Earth System Grid Federation*. https://doi.org/10.22033/ESGF/CMIP6.5771
Song, Z., Qiao, F., Bao, Y., Shu, Q., Song, Y., & Yang, X. (2019). FIO-QLNM FIO-ESM2.0 model output prepared for CMIP6 CMIP historical [Dataset]. *Earth System Grid Federation*. https://doi.org/10.22033/ESGF/CMIP6.9199
Swart, N. C., Cole, J. N., Kharin, V. V., Lazare, M., Scinocca, J. F., Gillett, N. P., et al. (2019a). CCCma CanESM5 model output prepared for CMIP6 CMIP historical [Dataset]. *Earth System Grid Federation*. https://doi.org/10.22033/ESGF/CMIP6.3610
Swart, N. C., Cole, J. N., Kharin, V. V., Lazare, M., Scinocca, J. F., Gillett, N. P., et al. (2019b). CCCma CanESM5 model output prepared for CMIP6 ScenarioMIP SSP245 [Dataset]. *Earth System Grid Federation*. https://doi.org/10.22033/ESGF/CMIP6.3685
Swart, N. C., Cole, J. N., Kharin, V. V., Lazare, M., Scinocca, J. F., Gillett, N. P., et al. (2019c). CCCma CanESM5 model output prepared for CMIP6 ScenarioMIP ssp585 [Dataset]. *Earth System Grid Federation*. https://doi.org/10.22033/ESGF/CMIP6.3696
Tang, Y., Rumbold, S., Ellis, R., Kelley, D., Mulcahy, J., Sellar, A., et al. (2019). MOHC UKESM1.0-LL model output prepared for CMIP6 CMIP historical [Dataset]. *Earth System Grid Federation*. https://doi.org/10.22033/ESGF/CMIP6.6113
Tatebe, H., & Watanabe, M. (2018). MIROC MIROC6 model output prepared for CMIP6 CMIP historical [Dataset]. *Earth System Grid Federation*. https://doi.org/10.22033/ESGF/CMIP6.5603
Voldoire, A. (2018). CMIP6 simulations of the CNRM-CERFACS based on CNRM-CM6-1 model for CMIP experiment historical [Dataset]. *Earth System Grid Federation*. https://doi.org/10.22033/ESGF/CMIP6.4066
Voldoire, A. (2019a). CNRM-CERFACS CNRM-CM6-1-HR model output prepared for CMIP6 CMIP historical [Dataset]. *Earth System Grid Federation*. https://doi.org/10.22033/ESGF/CMIP6.4067
Voldoire, A. (2019b). CNRM-CERFACS CNRM-CM6-1-HR model output prepared for CMIP6 ScenarioMIP SSP245 [Dataset]. *Earth System Grid Federation*. https://doi.org/10.22033/ESGF/CMIP6.4190
Voldoire, A. (2019c). CNRM-CERFACS CNRM-CM6-1-HR model output prepared for CMIP6 ScenarioMIP ssp585 [Dataset]. *Earth System Grid Federation*. https://doi.org/10.22033/ESGF/CMIP6.4225
Voldoire, A. (2019d). CNRM-CERFACS CNRM-CM6-1 model output prepared for CMIP6 ScenarioMIP SSP245 [Dataset]. *Earth System Grid Federation*. https://doi.org/10.22033/ESGF/CMIP6.4189
Voldoire, A. (2019e). CNRM-CERFACS CNRM-CM6-1 model output prepared for CMIP6 ScenarioMIP ssp585 [Dataset]. *Earth System Grid Federation*. https://doi.org/10.22033/ESGF/CMIP6.4224
Volodin, E., Mortikov, E., Gritsun, A., Lykossov, V., Galin, V., Diansky, N., et al. (2019a). INM INM-CM4-8 model output prepared for CMIP6 CMIP historical [Dataset]. *Earth System Grid Federation*. https://doi.org/10.22033/ESGF/CMIP6.5069
Volodin, E., Mortikov, E., Gritsun, A., Lykossov, V., Galin, V., Diansky, N., et al. (2019b). INM INM-CM5-0 model output prepared for CMIP6 CMIP historical [Dataset]. *Earth System Grid Federation*. https://doi.org/10.22033/ESGF/CMIP6.5070
Volodin, E., Mortikov, E., Gritsun, A., Lykossov, V., Galin, V., Diansky, N., et al. (2019c). INM INM-CM5-0 model output prepared for CMIP6 ScenarioMIP SSP245 [Dataset]. *Earth System Grid Federation*. https://doi.org/10.22033/ESGF/CMIP6.12328
Volodin, E., Mortikov, E., Gritsun, A., Lykossov, V., Galin, V., Diansky, N., et al. (2019d). INM INM-CM5-0 model output prepared for CMIP6 ScenarioMIP SSP585 [Dataset]. *Earth System Grid Federation*. https://doi.org/10.22033/ESGF/CMIP6.12338
Wieners, K.-H., Giorgetta, M., Jungclaus, J., Reick, C., Esch, M., Bittner, M., et al. (2019a). MPI-M MPI-ESM1.2-LR model output prepared for CMIP6 CMIP historical [Dataset]. *Earth System Grid Federation*. https://doi.org/10.22033/ESGF/CMIP6.6595
Wieners, K.-H., Giorgetta, M., Jungclaus, J., Reick, C., Esch, M., Bittner, M., et al. (2019b). MPI-M MPI-ESM1.2-LR model output prepared for CMIP6 ScenarioMIP SSP245 [Dataset]. *Earth System Grid Federation*. https://doi.org/10.22033/ESGF/CMIP6.6693
Wieners, K.-H., Giorgetta, M., Jungclaus, J., Reick, C., Esch, M., Bittner, M., et al. (2019c). MPI-M MPI-ESM1.2-LR model output prepared for CMIP6 ScenarioMIP ssp585 [Dataset]. *Earth System Grid Federation*. https://doi.org/10.22033/ESGF/CMIP6.6705
Wu, T., Chu, M., Dong, M., Fang, Y., Jie, W., Li, J., et al. (2018). BCC BCC-CSM2MR model output prepared for CMIP6 CMIP historical [Dataset]. *Earth System Grid Federation*. https://doi.org/10.22033/ESGF/CMIP6.2948
Yukimoto, S., Koshiro, T., Kawai, H., Oshima, N., Yoshida, K., Urakawa, S., et al. (2019a). MRI MRI-ESM2.0 model output prepared for CMIP6 CMIP historical [Dataset]. *Earth System Grid Federation*. https://doi.org/10.22033/ESGF/CMIP6.6842
Yukimoto, S., Koshiro, T., Kawai, H., Oshima, N., Yoshida, K., Urakawa, S., et al. (2019b). MRI MRI-ESM2.0 model output prepared for CMIP6 ScenarioMIP SSP245 [Dataset]. *Earth System Grid Federation*. https://doi.org/10.22033/ESGF/CMIP6.6910
Yukimoto, S., Koshiro, T., Kawai, H., Oshima, N., Yoshida, K., Urakawa, S., et al. (2019c). MRI MRI-ESM2.0 model output prepared for CMIP6 ScenarioMIP ssp585 [Dataset]. *Earth System Grid Federation*. https://doi.org/10.22033/ESGF/CMIP6.6929